



UPPSALA
UNIVERSITET

*Digital Comprehensive Summaries of Uppsala Dissertations
from the Faculty of Science and Technology 1541*

Electronic structure investigations of transition metal complexes through X-ray spectroscopy

MEIYUAN GUO



ACTA
UNIVERSITATIS
UPSALIENSIS
UPPSALA
2017

ISSN 1651-6214
ISBN 978-91-513-0035-1
urn:nbn:se:uu:diva-328072

Dissertation presented at Uppsala University to be publicly examined in Polhemssalen, Ång/10134, Ångströmlaboratoriet, Lägerhyddsvägen 1, Uppsala, Friday, 6 October 2017 at 09:30 for the degree of Doctor of Philosophy. The examination will be conducted in English. Faculty examiner: H el ene Bolvin (The Laboratoire de Chimie et Physique Quantiques (LCPQ)).

Abstract

Guo, M. 2017. Electronic structure investigations of transition metal complexes through X-ray spectroscopy. *Digital Comprehensive Summaries of Uppsala Dissertations from the Faculty of Science and Technology* 1541. 73 pp. Uppsala: Acta Universitatis Upsaliensis. ISBN 978-91-513-0035-1.

Catalysts based on the first-row (*3d*) transition metals are commonly seen in chemical and biological reactions. To understand the role of the transition metal in the catalyst, the element specific technique core level spectroscopy is used to probe the electronic structure and geometric properties centered around the metal site. Different types of X-ray spectra can be applied to probe the metal *3d* character orbitals involved in reactions, which make it possible to identify and characterize the reactive sites of samples in different forms. A detailed interpretation and understanding of the different X-ray spectra requires a unified method which can be used to model different types of X-ray spectra, e.g., soft and hard X-rays. In this thesis, theoretical investigations of the electronic structures of *3d* transition metal complexes through X-ray spectroscopy are presented. The restricted active space method (RAS) is used to successfully reproduce different types of X-ray spectra by including all important spectral effects: multiplet structures, spin-orbit coupling, charge-transfer excitations, ligand field splitting and *3d-4p* orbital hybridization. Different prototypes of molecules are adopted to test the applicability of the RAS theory.

The metal L edge X-ray absorption (XAS) spectra of low spin complexes $[Fe(CN)_6]^n$ and $[Fe(P)(ImH)_2]^n$ in ferrous and ferric oxidation state are discussed. The RAS calculations on iron L edge spectra of these comparing complexes have been performed to fingerprint the oxidation states of metal ion, and different ligand environments. The *Fe(P)* system has several low-lying spin states in the ground state, which is used as a model to identify unknown species by their spectroscopic fingerprints through RAS spectra simulations. To pave the route of understanding the electronic structure of oxygen evolution complex of Mn_4CaO_5 cluster, the $Mn^{II}(acac)_2$ and $Mn^{III}(acac)_3$ are adopted as prototypical Mn-complexes. The *3d* partial fluorescence yield-XAS are employed on the Mn L-edge in solution. Combining experiments and RAS calculations, primary questions related to the oxidation state and spin state are discussed.

The first application to simulate the metal K pre-edge XAS of mono-iron complexes and iron dimer using RAS method beyond the electric dipole is completed by implementing the approximate origin independent calculations for the intensities. The K pre-edge spectrum of centrosymmetric complex $[FeCl_6]^n$ ferrous state is discussed as s and a donor model systems. The intensity of the K pre-edge increases significantly if the centrosymmetric environment is broken, e.g., when going from a six-coordinate to the four-coordinate site in $[FeCl_4]^n$. Distortions from centrosymmetry allow for *3d-4p* orbital hybridization, which gives rise to electric dipole-allowed transitions in the K pre-edge region. In order to deliver ample electronic structure details with high resolution in the hard X-ray energy range, the two-photon *1s2p* resonant inelastic X-ray scattering process is employed. Upon the above successful applications of one-photon iron L edge and K pre-edge spectra, the RAS method is extended to simulate and interpret the *1s2p* resonant inelastic X-ray scattering spectra of $[Fe(CN)_6]^n$ in ferrous and ferric oxidation states. The RAS applications on X-ray simulations are not restricted to the presented spectra in the thesis, it can be applied to the photon process of interest by including the corresponding core and valence orbitals of the sample.

Keywords: transition metal complexes, x-ray spectroscopy, electronic structures

Meiyuan Guo, Department of Chemistry - Ångstr om, Theoretical Chemistry, Box 518, Uppsala University, SE-75120 Uppsala, Sweden.

  Meiyuan Guo 2017

ISSN 1651-6214

ISBN 978-91-513-0035-1

urn:nbn:se:uu:diva-328072 (<http://urn.kb.se/resolve?urn=urn:nbn:se:uu:diva-328072>)

*Home is behind, the world ahead,
And there are many paths to tread
Through shadows to the edge of night,
 Until the stars are all alight.
Then world behind and home ahead,
We will wander back and home to bed.
Mist and twilight, cloud and shade,
 Away shall fade! Away shall fade!*

J.R.R. Tolkien

List of papers

This thesis is based on the following papers.

- I **Restricted active space calculations of L-edge X-ray absorption spectra: From molecular orbitals to multiplet states**
Rahul V Pinjari, Mickaël G Delcey, Meiyuan Guo, Michael Odelius and Marcus Lundberg. *J. Chem. Phys.*, 141,124116 (2014), DOI: 10.1063/1.4896373
- II **Cost and sensitivity of restricted active space calculations of metal L-edge X-ray absorption spectra**
Rahul V Pinjari, Mickaël G Delcey, Meiyuan Guo, Michael Odelius and Marcus Lundberg. *J. Comput. Chem.*, 37, 477 (2016), DOI: 10.1002/jcc.24237
- III **Fingerprinting electronic structures of heme using theoretical modeling of L-edge X-ray absorption spectra**
Meiyuan Guo, Erik Källman, Rahul V Pinjari, and Marcus Lundberg. Manuscript.
- IV **Probing the oxidation state: A case study of $Mn^{II}(acac)_2$ and $Mn^{III}(acac)_3$ on how charge and spin densities determine Mn L-edge X-ray absorption energies**
Markus Kubin*, Meiyuan Guo*, Thomas Kroll, Heike Löchel, Erik Källman, Michael L. Baker, Rolf Mitzner, Jan Kern, Alexander Föhlisch, Alexei Erko, Uwe Bergmann, Vittal Yachandra, Junko Yano, Marcus Lundberg, Philippe Wernet. Manuscript.
- V **Simulations of iron K pre-edge X-ray absorption spectra using the restricted active space method**
Meiyuan Guo, Lasse Kragh Sørensen, Mickaël G Delcey, Rahul V Pinjari and Marcus Lundberg. *Phys. Chem. Chem. Phys.*, 18, 3250 (2016), DOI: 10.1039/C5CP07487H
- VI **Applications to metal K pre-edges of transition metal dimers illustrate the approximate origin independence for the intensities in the length representation.**
Lasse Kragh Sørensen, Meiyuan Guo, Roland Lindh, and Marcus Lundberg. *Mol. Phys.*, 115, 174 (2016), DOI: 10.1080/00268976.2016.1225993

**VII Molecular orbital simulations of metal 1s2p resonant inelastic
X-ray scattering**

Meiyuan Guo, Erik Källman, Lasse Kragh Sørensen, Mickaël G
Delcey, Rahul V Pinjari and Marcus Lundberg. *J. Phys. Chem. A*, 120,
5848 (2016), DOI: 10.1021/acs.jpca.6b05139

*Authors contributed equally to this work.

Reprints were made with permission from the publishers.

Comments on my own contribution

- I Performed the multiplet calculations, and took part in analysing the results.
- II Performed the calculations of convergence dependence on the number of final states, RASPT2 calculations with correlated core orbitals and took part in analysing the results.
- III Participated in the design of the study, had the main responsibility for the RAS calculations and the analysis, and took part in writing the manuscript.
- IV Participated in the design of the study, had the main responsibility for the RAS calculations and the analysis, and took part in writing the manuscript.
- V Participated in the design of the study, had the main responsibility for the RAS calculations and the analysis, and took part in writing the manuscript.
- VI Participated in the design of the study, took part in discussion and analysis of results.
- VII Participated in the design of the study, had the main responsibility for the RAS calculations and the analysis, and took part in writing the manuscript.

Publications that are left out of the thesis

The following is a list of papers to which I have contributed but are left out of this thesis.

1. **Tungsten Hydrides with Pendant Pyridyl Functional Groups and Their Tunable Intramolecular Proton-Coupled Electron Transfer**
Tianfei Liu, Meiyuan Guo, Andreas Orthaber, Reiner Lomoth, Marcus Lundberg, Sascha Ott and Leif Hammarström. Submitted.
2. **L2,3-edge 3d-Partial-fluorescence yield X-ray absorption as a sensitive probe of a distorted symmetry**
Meiyuan Guo, Marcus Lundberg, and Piter S. Miedema. Manuscript.
3. **Valence orbital interactions and d-d excitations in hard X-ray resonant inelastic X-ray scattering: Revisiting manganese hexacyanide**
Meiyuan Guo, Erik Källman, Lasse Kragh Sørensen, Marcus Lundberg. Manuscript.
4. **Valence electronic states of a dilute Chromium(III) complex in solution accessed by 2p-3d Cr L-edge absorption spectroscopy**
Markus Kubin, Meiyuan Guo, Maria Ekimova, Vittal Yachandra, Junko Yano, Erik Nibbering, Marcus Lundberg, Philippe Wernet. Manuscript.
5. **Quantifying soft x-ray dose-dependent sample damage to redox-active Mn(III) species in solution using Mn L-edge spectroscopy**
Markus Kubin, Meiyuan Guo, Jan Kern, Brian O' Cinneide, Alexander Föhlisch, Vittal Yachandra, Marcus Lundberg, Junko Yano, Philippe Wernet. Manuscript.
6. **Direct probing of 2p-3d x-ray absorption cross-sections of dilute Mn complexes in solution using an in-vacuum transmission flat-jet**
Markus Kubin, Maria Ekimova, Meiyuan Guo, Marcus Lundberg, Vittal Yachandra, Junko Yano, Erik Nibbering, Philippe Wernet. Manuscript.

Abbreviations

ADP	A denosine D i- P hosphate
ATP	A denosine T ri- P hosphate
NADP+	N icotinamide A denine D inucleotide P hosphate oxidase
HF	H artree- F ock
SOC	S pin O rbital C oupling
MCSCF	M ulti- C onfiguration S elf C onsistent F ield
CSF	C onfiguration S tate F unctions
RASSI	R estricted A ctive S pace S tate I nteraction
CAS	C omplete A ctive S pace
RAS	R estricted A ctive S pace
XAS	X -ray A bsorption S pectroscopy
PFY	P artial F luorescence Y ield
TEY	T otal E lectron Y ield
RIXS	R esonant I nelastic X -ray S cattering
DFT	D ensity F unctional T heory
CTM	C harge T ransfer M ultiplet
ROCIS	R estricted O pen-shell C onfiguration I nteraction with S ingles
ES	E xcited S tate
GS	G round S tate
CS	C osine S imilarity
PT2	S econd-order P erturbation T heory
LMCT	L igand M etal C harge T ransfer
MLCT	M etal L igand C harge T ransfer
MS	M ulti- S tate
SS	S tate S pecific
PCM	P olarizable C ontinuum M odel
CCD	C harge C oupled D evice
CIE	C onstant I ncident E nergy
CEE	C onstant E mission E nergy
OEC	O xygen E volution C atalyst
RCD	R adial C harge D ensity
RSD	R adial S pin D ensity

Contents

1	Introduction	13
2	Core level spectroscopy	16
2.1	The role of metal 3d orbitals	16
2.2	Probe metal 3d orbitals of catalysts	17
2.2.1	X-ray absorption spectroscopy	17
2.2.2	Resonant inelastic X-ray spectroscopy	19
3	Computational framework	22
3.1	Born-Oppenheimer approximation	22
3.2	Hartree-Fock theory	23
3.3	Multi-configurational method	25
3.3.1	Second-order perturbation	26
3.3.2	RAS method for X-ray spectra	28
3.4	Charge transfer multiplet model	29
3.5	Other methods for modelling X-ray spectra	30
4	Soft X-rays	32
4.1	Atomic calculation of low-spin Fe^{3+}	32
4.2	Metal L-edge XAS of low-spin iron complexes	34
4.2.1	Fingerprint the oxidation states	35
4.2.2	Fingerprint the ligand environment	36
4.2.3	Fingerprint the different electronic states	36
4.2.4	Cost and stability of RAS method	39
4.2.5	Summary	39
4.3	PFY-XAS of manganese complexes	40
4.3.1	PFY-XAS of $Mn^{II}(acac)_2$ and $Mn^{III}(acac)_3$	41
4.3.2	Spin and charge density	42
4.3.3	Origin of the spectral shape and edge shift	44
4.3.4	Summary	44
5	Hard X-rays	46
5.1	Metal K pre-edge XAS	46
5.1.1	Multiplet structures	47
5.1.2	Hybridization of dipole and quadrupole contributions ..	48
5.1.3	Back-donation charge transfer	50
5.1.4	Summary	51
5.2	Simulations of the metal 1s2p RIXS of $[Fe(CN)_6]^{n-}$	52
5.2.1	The 1s2p RIXS spectra of $[Fe(CN)_6]^{4-}$	53

5.2.2	The 1s2p RIXS spectra of $[Fe(CN)_6]^{3-}$	55
5.2.3	Summary	56
6	Conclusion and outlook	58
7	Sammanfattning på svenska	60
	Acknowledgements	63
	References	65

1. Introduction

The increasing population together with increasing living standard boosts the energy consumptions of fossil fuels, such as coal, oil, and natural gas, which in turn boosts the emissions of CO_2 , CO , NO_x , and other hazardous air pollutants from the combustion of fossil fuels. These energy sources have limited reserves and will dwindle in the foreseeable future. The consumptions are adversely affecting our environment and human health. The CO_2 emission is widely considered as the main factor that contributes to climate change, such as the increased average global temperature, the increased sea level, declined mountain glaciers and snow cover and many other observed changes. The urgent circumstance forces us to find alternative inexhaustible, renewable and green energy sources, such as hydro, biofuels, geothermal, wind, and solar energy, *etc.* Among all these green energies, solar energy is the most attractive alternative energy source and can compete with fossil fuels.[1, 2]

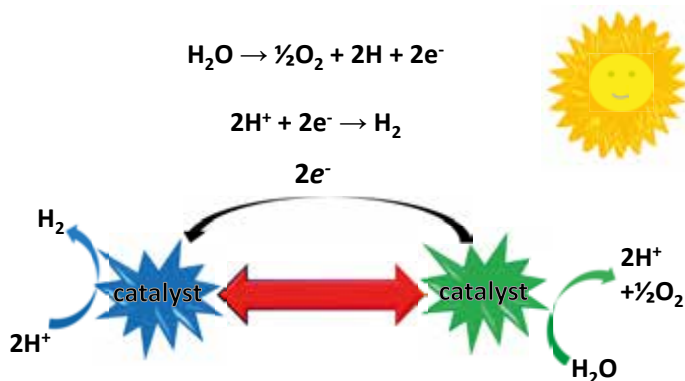


Figure 1.1. The scheme of splitting water into O_2 and H_2 using catalyst.

The natural photosynthetic process occurring in plant and algae shows us a perfect example how to utilize the solar energy.[3] There are two component sets of reactions that occur sequentially: light reactions and dark reactions.[2, 4, 5] In the light reactions, the sunlight is firstly absorbed by the light-harvest systems and converted into electrochemical energy (or redox equivalents),

then a water oxidation complex uses this redox potential to catalyze conversion of water to O_2 , hydrogen ions, and electrons stored as reducing equivalents, at the same time, the oxidizing agent $NADP^+$ is reduced. Secondly, phosphorylation takes place leading to the formation of ATP. This involves the capture of some part of the radiant energy by phosphorylating ADP to produce ATP. In the dark reactions, the CO_2 is reduced to carbohydrate.

Inspired by the natural photosynthesis process, much effort has been dedicated to using sunlight directly as the energy source for water splitting.[5, 6] In such process, the water is oxidised to O_2 , and then the electrons can be used to make fuel such as H_2 , methanol, methane, carbohydrates, or other fuels, which can be stored for later use.[7, 8]

When restricted to H_2 and O_2 evolution from water and sunlight, it falls into the category of light-driven water splitting.[9–12] Usually the processes are accelerated by using expensive noble metals (such as platinum, ruthenium, iridium and rhodium) acting as water oxidation catalysts and hydrogen reduction catalysts.[11, 13] However, these metals are not themselves sustainable resources, and lots of suitable catalysts are required in order to generate useful amount of hydrogen on practical timescale. So the viability of water oxidation and hydrogen evolution relies on the design of novel, efficient and robust catalytic materials based on earth-abundant and cheap metals. Recently lots of attention have been given to the design of catalysts based on the first-row transition metals, including nickel, cobalt, iron, copper and manganese.[13–15] However, none of the present catalysts satisfy the industrial requirements of stability, efficiency and speed. In order to design catalysts that fulfill the above requirements, inspiration can be drawn from the reaction and the active site in the natural photosynthesis process, e.g, the four-electron redox reaction occurring in the Mn_4CaO_5 cluster. Moreover, better knowledge about the electronic structures as well as geometric information of transition metal catalysts themselves is also required.

X-ray spectroscopy is an essential method that can offer a unique probe of the local geometric and electronic structure of the element of interest, which are not observable in optical spectroscopy.[16] Optical spectroscopy generally gives a picture of the total chemical bonding interactions, and not particular for the metal $3d$ orbitals, a limitation that also applies to other spectroscopy techniques, e.g., electron paramagnetic resonance, magnetic circular dichroism, and resonance Raman. An electron can absorb a particular energy and then be excited to empty or partially filled orbitals just below the ionization potential giving an edge, see Figure 1.2, which contains information about the targeted orbitals. The energy of the absorption edge provides information about the oxidation and spin state of the absorbing element. The choice of the energy of the X-ray determines the specific element being probed. As we are interested in $3d$ transition metal catalysts, the metal L-edge spectra (electric dipole transition) can be directly used to probe the metal $3d$ orbitals, however, its applications are largely dependent on different detection schemes.[17–20]

The light elements (e.g, carbon, nitrogen and oxygen) have intense K-edge absorption in the soft energy region, which can have strong background contribution to the metal L-edge spectra and increase radiation damage.[21] To avoid the limitations of measurement on dilute samples such as catalysts, biological samples, or environmental samples, X-ray absorption spectroscopy (XAS) can be measured as fluorescence yield spectra,[20, 22] or alternatively use hard X-rays at the metal K edge region.[23]

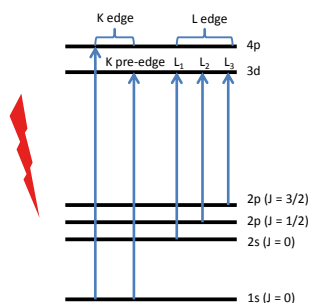


Figure 1.2. The energy level diagram for K edge transitions ($1s \rightarrow 3d/4p$), and L-edge (L_1 , L_2 , and L_3) transitions ($2s/2p \rightarrow 3d$). The energy levels are not drawn to scale.

A detailed interpretation and understanding of the X-ray spectra requires accurate simulations, which can unravel subtle spectral features. To model the X-ray spectra, one high-level method that can describe important spectral effects, e.g, 2p and 3d spin orbit coupling (SOC), multiplet structures, selection rule, and charge transfer between metal and ligands,[24–27] is required. One of main focus of this following thesis is to calculate and interpret the metal L-edge XAS measured as transmission and fluorescence yield spectra in gas phase and in solution. Another main focus is to model hard X-rays. For the metal K pre-edge XAS, the intensity calculations have to be implemented beyond the electric dipole transitions. Upon successful calculations on metal K pre-edge and metal L edge, it is possible to describe the high resolution hard X-ray spectra - $1s2p$ resonant inelastic X-ray scattering (RIXS). The calculations of X-ray spectra in different energy regions and in different photon processes would be useful in interpreting X-ray spectra and fingerprinting the electronic structures of solution catalysts and enzymes.

2. Core level spectroscopy

The electrons of an atom can be divided into two categories: inner shell (core) electron and outer shell (valence) electrons. The properties of the transition metal catalysts are dominated by the valence electrons that participate in their chemical bond formations and interactions. The core-electrons are localized around the nucleus, and they do not take part in the formation of a chemical bond and can be considered inert. It is clear that the study of the valence electronic structure can offer information on the nature of the chemical bond. However, core electrons provide a method to locally study the valence electronic structure and geometric properties centered around one atomic site, which is one of the unique properties of core level spectroscopy methods.

2.1 The role of metal 3d orbitals

The 3d transition metals are characterized by their capability to form cations with incomplete valence sub-shells. The property of a transition metal complex involving in catalysis reaction depends on the orbital interaction between ligand orbitals and metal valence 3d orbitals. Taking a d^5 transition metal in the case of no ligand field, the five 3d orbitals are all singly occupied due to the electron-electron repulsion and Hund's rule.[28] The maximized spin is given, leading to a sextet state. The weak (octahedral coordinated) ligand-field strength lifts degeneracy of the 3d orbitals and still gives high spin ${}^6A_{1g}$ but with two subsets of near-degenerate orbitals, t_{2g} (d_{xy} , d_{xz} , d_{yz}) and e_g ($d_{x^2-y^2}$, d_{z^2}). The magnitude of the splitting is described in ligand field theory by the parameter of 10Dq.[29] When the ligand-field strength is further increased to surpass the spin pairing energy, the ${}^2T_{2g}$ state becomes the ground state, see Figure 2.1. The degeneracy of the three t_{2g} orbitals can be further removed due to the uneven electron occupation, which can be simply described as Jahn-Teller effects.[30, 31] The Jahn-Teller theorem indicates that a state without degenerate orbitals is preferred over a state with such a degeneracy. This can result in the distortion of the symmetry, e.g. change the bond length along one axis.

It is shown that the occupations of the 3d-orbitals are dependent on the properties of the ligands.[32–35] In the metal-ligand molecular complexes, the molecular orbitals are formed as a linear combination between the metal valence orbitals (3d, 4s, and 4p) and ligand orbitals (σ , π , σ^* , π^*). The orbital interactions between the orbitals of metal and the ligands would be dependent on their symmetry.

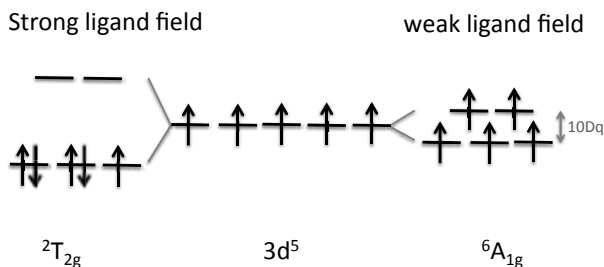


Figure 2.1. Simplified orbital diagrams of octahedral d^5 transition metal with weak and strong ligand field.

2.2 Probe metal 3d orbitals of catalysts

2.2.1 X-ray absorption spectroscopy

Modelling systems with well known structures have been very important to understand the XAS of catalysts and metallo-proteins.[16, 36–40] As now we are interested in 3d transition metals, the metal valence 3d orbitals play an important role during the catalytic reactions. To probe the 3d orbital contribution to bonding, the metal L-edge ($2p \rightarrow 3d$) XAS can be adopted to directly offer element-specific details of the metal 3d orbitals which are not observable in optical spectroscopy. For metal L-edge, a $2p^5$ core hole is created after electric dipole allowed $2p \rightarrow 3d$ transition, which creates a characteristic absorption peak namely L-edge, see Figure 2.2. The $2p^5$ core hole has a spin angular momentum $S = 1/2$ which can couple to the orbital angular momentum $L = 1$ and produce $J = 3/2$ and $J = 1/2$ final states, see Figure 2.2. These final states ($2p^5 3d^{n+1}$) are directly observable in the L-edge spectrum as two main regions called L_3 and L_2 edge, split by 2p SOC, see Figure 2.2.

For the first-row transition metals, the energies of L-edges lie in the energy region from ~ 400 to 1000 eV,[21] which may have strong K-edge absorption from light elements (carbon, nitrogen or oxygen). Due to the limitations on the sample environment, the uses of the metal L-edges XAS for transition metal catalysts are largely dependent on different detection schemes.[17–20] Transmission XAS involves measurement of the incident X-rays and the transmitted flux through the sample. In principle, this approach can be performed on any type of sample (gas, liquid, solid) provided the thickness and concentration is controllable. However, for dilute measurements the signal-to-noise ratio is

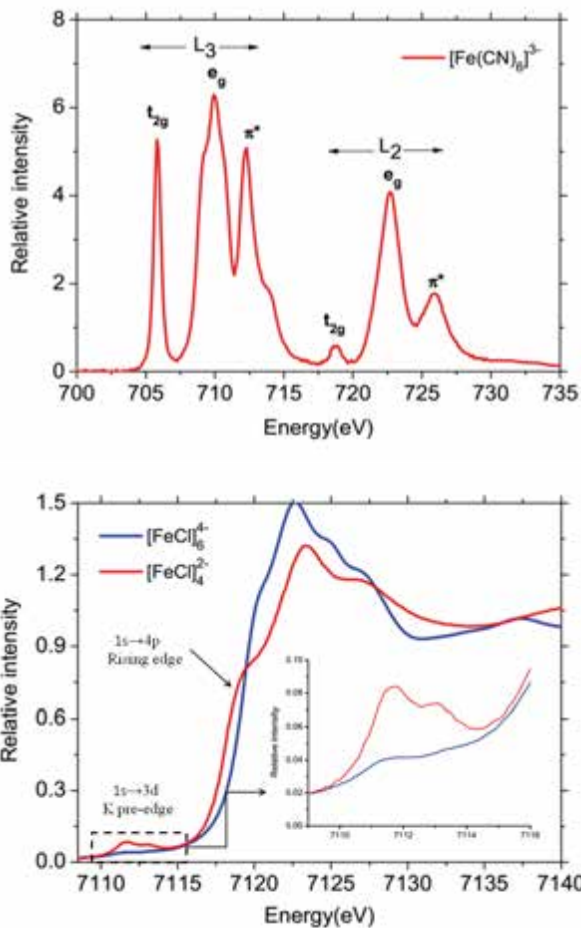


Figure 2.2. Upper: the experimental L-edge XAS of $[\text{Fe}(\text{CN})_6]^{3-}$. [41] below: the K-edge XAS of centrosymmetric complex $[\text{FeCl}_6]^{4-}$ and non-centrosymmetric complex $[\text{FeCl}_4]^{2-}$, [42] the K pre-edge and rising edge are marked.

typically poor. To avoid the limitations of transmission, XAS can be measured as fluorescence yield spectra. This is particularly important for dilute samples such as catalysts, biological samples, or environmental samples. [20, 22] In most cases, the sample will emit a variety of X-rays, both the fluorescence X-rays of interest and a background of K_α fluorescence from light elements. It is possible to discriminate the photons with respect to their energy and collect signals selectively by a detector, [20] the resulting spectrum is partial fluorescence yield XAS (PFY-XAS). The characteristics of the two different measurements are presented in the Table 2.1.

In order to avoid the limitations in sample environment, we could also alternatively use hard X-rays at the metal K edge region, [23] which provides

	Transmission	Fluorescence Yield
Sample Thickness	Thin	Thick/Any
Background	High	Low
Sensitivity	Bulk	Bulk
Sample Concentration	High	low/Any

Table 2.1. *The characteristics of transmission and fluorescence yield measurement technique.*

more freedom with respect to the sample environment. The advantage comes from the nature of 2 orders of magnitude smaller absorption cross section at the K edge, which can reduce radiation damage, and guarantees inherent bulk sensitivity due to the larger penetration depth, and thus results in simpler experimental setups compared to L-edge spectroscopy experiments. The main contribution to the K-edge spectrum is from metal $1s \rightarrow np$ transitions, where np represents the unoccupied p orbitals of the targeting metal element, see Figure 2.2. For probing the $3d$ orbital of transition metals, additional insights can be acquired by examining the features of the K pre-edge XAS. Both the energy and intensity of the pre-edge features are highly sensitive to the metal $3d$ character orbitals, see Figure 2.2. The K pre-edge characters are usually associated with the electron transition from core $1s$ orbital to unoccupied or partially occupied $3d$, and generate the $1s^1 3d^{n+1}$ final core excited states. The intensity of K pre-edge XAS can be largely increased when the centrosymmetric environment is broken (e.g., changing the coordination number) as distortions from centrosymmetry allow for metal $4p$ character to delocalize into metal $3d$ orbitals through their mutual interactions with the ligand orbitals. This $3d - 4p$ orbital hybridization is an important intensity mechanism as it gives rise to electric dipole-allowed transitions in the K pre-edge XAS.[42, 43] The admixture of $3d$ and $4p$ largely depends on the site symmetry, which could be easily interpreted using group point theory.[44] Usually the electric quadrupole transition is ~ 2 orders of magnitude weaker than a electric dipole transition. Que and co-workers showed that the iron K pre-edge XAS intensity has a near linear correlation with the total amount of metal $4p$ components in the $3d$ -type molecular orbitals.[45, 46] It is thus essential to be able to estimate the electric dipole allowed contributions when a catalyst site changes during a reaction.

2.2.2 Resonant inelastic X-ray spectroscopy

However, the metal K pre-edge features are not well resolved due to the short lifetime of the $1s$ core hole, which gives a large natural bandwidth.[47] One possible solution is to use $1s2p$ RIXS, because the resolution in the energy transfer direction is determined only by the lifetime of the final state, not the lifetime of the $1s$ core hole in the intermediate state.[23, 48] The $1s2p$ RIXS

event can be thought of as a two-step process, the general energy scheme is presented in Figure 2.3. Starting from the initial state, one $1s$ electron

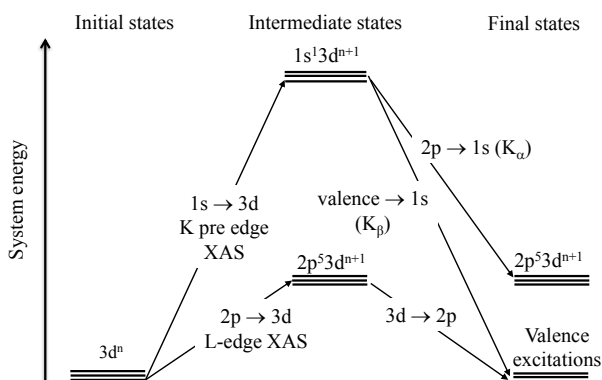


Figure 2.3. The scheme for different types of one-photon process XAS, and two-photon process RIXS.

is excited into an unoccupied or partial occupied $3d$ orbital via a electric quadrupole allowed transition, and subsequent electric dipole allowed decay of a $2p$ electron into the $1s$ hole, is detected by its photon emission. In a simplified picture the absorption process gives information of the partial occupied or empty orbitals, while the emission gives information about the partial occupied and doubly occupied orbitals. Metal L-edge absorption and $1s2p$ RIXS reach the same electron configurations of final states, and allow a direct comparison but with complementary selection rules. Recently, high-resolution RIXS spectra have been used to get detailed electronic structure information, *e.g.* the $3d$ orbital covalency, using hard X-rays.[49–51] With RIXS experiments reaching 0.1 eV resolution in the energy transfer direction,[52] it becomes important to describe both multiplet effects and charge-transfer features in the hard energy region.

To model X-ray spectra for general transition metal catalysts, there is a need for a high-level method that can describe the $2p$ and $3d$ SOC, electron correlation, and charge transfer between metal and ligands.[24–27] One such class of methods is the multi-configurational self consistent field (MCSCF) method.[53–57] Among which the most commonly adopted is the restricted active space self consistent field (RASSCF) method.[58] In calculations, the most important orbitals are included in the active space. Not only the metal

character core orbitals and $3d$ molecular orbitals, but also the important ligand molecular orbitals.

3. Computational framework

The recent experimental X-ray techniques progress can provide subtle spectral features, which imply that advanced quantum mechanism methods are required to accurately simulate and interpret the core level spectra. In this chapter, the important approximations and theory used to simulate the X-ray spectroscopies are introduced.

3.1 Born-Oppenheimer approximation

The nucleus has a much larger mass and much smaller velocity compared to the electron, assuming the motions of the nuclei can be ignored when describing the electrons in a molecule, and then the electron wave function depends upon the nuclei positions but not upon their velocities. This assumption is known as Born-Oppenheimer approximation,[59] which make it possible to simplify the complicated Schrödinger equation of a molecule. The nucleus and electron problems can be solved with independent wavefunctions from the separation of the nucleus and the electron motion.

The Schrödinger equation can be written as:

$$\hat{H}(\mathbf{r}, \mathbf{R})\Psi(\mathbf{r}, \mathbf{R}) = E(\mathbf{r}, \mathbf{R})\Psi(\mathbf{r}, \mathbf{R}) \quad (3.1)$$

The molecular wavefunction Ψ in the Born-Oppenheimer approximation can be separated into a product of nuclear and electronic components:

$$\Psi(\mathbf{r}, \mathbf{R}) = \psi_n(\mathbf{R})\psi_e(\mathbf{r}, \mathbf{R}) \quad (3.2)$$

where $\psi_n(\mathbf{R})$ is a wavefunction in terms of nuclear position, $\psi_e(\mathbf{r}, \mathbf{R})$ is electronic wavefunction in terms of the positions of electron and nuclei. The quantity \mathbf{r} represents the coordinates of all electrons, and \mathbf{R} represents coordinates of all nuclei.

Going back to the Eq.(3.1), the total molecular Hamiltonian can be written as

$$\hat{H}(\mathbf{r}, \mathbf{R}) = \hat{H}_n(\mathbf{R}) + \hat{H}_e(\mathbf{r}, \mathbf{R}) \quad (3.3)$$

where

$$\hat{H}_n(\mathbf{R}) = \hat{T}_n + V_{nn}(\mathbf{R}) \quad (3.4)$$

$$\hat{H}_e(\mathbf{r}, \mathbf{R}) = \hat{T}_e + V_{ee}(\mathbf{r}) + V_{en}(\mathbf{r}, \mathbf{R}) \quad (3.5)$$

Here \hat{T}_n is kinetic energy operator of the nuclei, $V_{nn}(\mathbf{R})$ is nuclei-nuclei repulsion Coulomb potential, \hat{T}_e is kinetic energy operator of the electron, $V_{ee}(\mathbf{r})$ is electron-electron repulsion Coulomb potential, and $V_{en}(\mathbf{r}, \mathbf{R})$ is electron-nuclei attraction Coulomb potential. Now substitute these terms and the Eq.(3.2) into the Schrödinger equation the Eq.(3.1), then obtain

$$(\hat{T}_n + V_{nn}(\mathbf{R}) + \hat{T}_e + V_{ee}(\mathbf{r}) + V_{en}(\mathbf{r}, \mathbf{R}))\Psi(\mathbf{r}, \mathbf{R}) = E(\mathbf{r}, \mathbf{R})\psi_n(\mathbf{R})\psi_e(\mathbf{r}, \mathbf{R}) \quad (3.6)$$

Consider the nuclei and electron kinetic energy operator acting on the wavefunction, \hat{T}_n contains derivatives in terms of nuclei coordinates, it has effects on both nuclei and electron wavefunction:

$$\hat{T}_n\psi_n(\mathbf{R})\psi_e(\mathbf{r}, \mathbf{R}) = \psi_n(\mathbf{R})\hat{T}_n\psi_e(\mathbf{r}, \mathbf{R}) + \psi_e(\mathbf{r}, \mathbf{R})\hat{T}_n\psi_n(\mathbf{R}) \quad (3.7)$$

Here, the $\hat{T}_n\psi_e(\mathbf{r}, \mathbf{R})$ is much smaller than $\hat{T}_n\psi_n(\mathbf{R})$, hence the Eq.(3.7) can be written as

$$\hat{T}_n\psi_n(\mathbf{R})\psi_e(\mathbf{r}, \mathbf{R}) \approx \psi_e(\mathbf{r}, \mathbf{R})\hat{T}_n\psi_n(\mathbf{R}) \quad (3.8)$$

\hat{T}_e contains derivatives in terms of electron coordinates, and hence it only has effect on the electron wavefunction,

$$\hat{T}_e\psi_e(\mathbf{r}, \mathbf{R})\psi_n(\mathbf{R}) = \psi_n(\mathbf{R})\hat{T}_e\psi_e(\mathbf{r}, \mathbf{R}) \quad (3.9)$$

Apply the same fact in the the Schrödinger equation the Eq.(3.1), it can be written as

$$\psi_e(\mathbf{r}, \mathbf{R})\hat{H}_n(\mathbf{R})\psi_n(\mathbf{R}) + \psi_n(\mathbf{R})\hat{H}_e(\mathbf{r}, \mathbf{R})\psi_e(\mathbf{r}, \mathbf{R}) = E(\mathbf{r}, \mathbf{R})\psi_n(\mathbf{R})\psi_e(\mathbf{r}, \mathbf{R}) \quad (3.10)$$

Then divide the both sides of Eq. (3.10) by $\psi_n(\mathbf{R})\psi_e(\mathbf{r}, \mathbf{R})$, which gives

$$\frac{\hat{H}_e(\mathbf{r}, \mathbf{R})\psi_e(\mathbf{r}, \mathbf{R})}{\psi_e(\mathbf{r}, \mathbf{R})} = E - \frac{\hat{H}_n(\mathbf{R})\psi_n(\mathbf{R})}{\psi_n(\mathbf{R})} \quad (3.11)$$

The right side depends only on the coordinates of nuclei \mathbf{R} , and can be written compactly as function $\varepsilon(\mathbf{R})$. Substitute it in Eq(3.11) and obtain the electronic Schrödinger equation:

$$\hat{H}_e(\mathbf{r}, \mathbf{R})\psi_e(\mathbf{r}, \mathbf{R}) = \varepsilon(\mathbf{R})\psi_e(\mathbf{r}, \mathbf{R}) \quad (3.12)$$

3.2 Hartree-Fock theory

The electronic Schrödinger equation was obtained from the Born-Oppenheimer approximation in section 3.1. The exact solution to the equation can only be reachable for one-electron systems, such as the hydrogen atom or hydrogen like systems. As long as one uses the electronic Schrödinger equation to

deal with a many-body problem in quantum chemistry, only approximated solutions can be obtained. Hartree-Fock theory is the simplest approximation method to solve many-body electronic Schrödinger equation.[60] It simplifies the N-electron problem into N one-electron problems. Hence, it is reasonable to start the wavefunction with a general form:

$$\Psi(\mathbf{r}_1, \mathbf{r}_2, \dots, \mathbf{r}_N) = \psi_1(\mathbf{r}_1)\psi_2(\mathbf{r}_2)\cdots\psi_N(\mathbf{r}_N) \quad (3.13)$$

when considering the full set of coordinates including space and spin, the Eq.(3.13) can be rewritten as

$$\Psi(\mathbf{X}_1, \mathbf{X}_2, \dots, \mathbf{X}_N) = \chi_1(\mathbf{X}_1)\chi_2(\mathbf{X}_2)\cdots\chi_N(\mathbf{X}_N) \quad (3.14)$$

Clearly, this wavefunction can not satisfy the Pauli principle, in which the wavefunction has to be antisymmetric. In order to fulfil the antisymmetry requirement, the wavefunction of the simplest two-electron many-body system can be written like below:

$$\Psi(\mathbf{X}_1, \mathbf{X}_2) = \frac{1}{\sqrt{2}}[\chi_1(\mathbf{X}_1)\chi_2(\mathbf{X}_2) - \chi_1(\mathbf{X}_2)\chi_2(\mathbf{X}_1)] \quad (3.15)$$

The wavefunction also can be represented using determinants like

$$\Psi(\mathbf{X}_1, \mathbf{X}_2) = \frac{1}{\sqrt{2}} \begin{vmatrix} \chi_1(\mathbf{X}_1) & \chi_2(\mathbf{X}_1) \\ \chi_1(\mathbf{X}_2) & \chi_2(\mathbf{X}_2) \end{vmatrix} \quad (3.16)$$

Now it is easy to expand the determinant for an N-electron system

$$\Psi(\mathbf{X}_1, \mathbf{X}_2, \dots, \mathbf{X}_N) = \frac{1}{\sqrt{N!}} \begin{vmatrix} \chi_1(\mathbf{X}_1) & \chi_2(\mathbf{X}_1) & \cdots & \chi_N(\mathbf{X}_1) \\ \chi_1(\mathbf{X}_2) & \chi_2(\mathbf{X}_2) & \cdots & \chi_N(\mathbf{X}_2) \\ \vdots & \vdots & \ddots & \vdots \\ \chi_1(\mathbf{X}_N) & \chi_2(\mathbf{X}_N) & \cdots & \chi_N(\mathbf{X}_N) \end{vmatrix} \quad (3.17)$$

The electronic Hamiltonian can be written in a simple way as

$$\hat{H}_e = \sum_i \zeta(\alpha) + \sum_{\alpha < \beta} \eta(\alpha, \beta) + V_{nn}(\mathbf{R}) \quad (3.18)$$

where $\zeta(\alpha)$ represents a one-electron operator, $\eta(\alpha, \beta)$ represents a two-electron operator, and $V_{nn}(\mathbf{R})$ is a constant for the fixed set of nuclei coordinates \mathbf{R} . Similarly, the electronic energy in terms of integrals can also be expressed using one-electron and two-electron operators:

$$E = \sum_{\alpha} \langle \alpha | \zeta | \alpha \rangle + \frac{1}{2} \sum_{\alpha\beta} ([\alpha\alpha|\beta\beta] - [\alpha\beta|\beta\alpha]) \quad (3.19)$$

where $\langle \alpha | \zeta | \alpha \rangle$ is one-electron integral, $[\alpha\alpha|\beta\beta]$ is two-electron Coulomb integral, $[\alpha\beta|\beta\alpha]$ is exchange integral, these integrals can be easily computed

by existing efficient computer algorithms. The energy difference between the exact non-relativistic energy of the system and the HF limit energy is called correlation energy. The electron correlation can be separated into two components namely static correlation and dynamical correlation,[61] both of which will be elaborated on in the following section.

3.3 Multi-configurational method

The static correlation can be well described by multi-configurational self consistent field (MCSCF) methods, among which the most widely adopted approaches is complete active space SCF (CASSCF).[53] The MCSCF wavefunction is written as a linear combination of Slater determinant or configuration state functions (CSF):

$$|\kappa, \mathbf{C}\rangle = \exp(-\hat{\kappa}) \sum_i C_i |i\rangle \quad (3.20)$$

The CSF can be selected as all possible ones formed within a given active space. Each CSF differs in how the electrons are placed in the molecular orbitals. The molecular orbitals are expanded in a basis of atomic orbitals. A MCSCF wavefunction is one in which both the configuration mixing coefficients and the molecular orbitals expansion coefficients are variationally optimized. The number of CSF can be calculated using Weyl's formula:

$$Q_{n,N,S} = \frac{2S+1}{n+1} \binom{n+1}{N/2-S} \binom{n+1}{N/2+S+1} \quad (3.21)$$

where n is the number of orbitals, and N is the number of electrons, and S is spin quantum number. The numbers of singlet states for N electrons in n orbitals are referenced below:

N/n	2	4	6	8	10	12	14	16
2	3	10	21	36	55	78	105	136
4	1	20	105	336	825	1716	3185	5440
6	-	10	175	1176	4950	15730	41405	95200
8	-	1	105	1764	13860	70785	273273	866320
10	-	-	21	1176	19404	169884	1002001	4504864
12	-	-	1	336	13860	226512	2147145	14158144
14	-	-	-	36	4950	169884	2760615	27810640
16	-	-	-	1	825	70785	2147145	34763300

Table 3.1. The number of singlet states for N electrons in n orbitals.

For the open shell $3d$ transition metal complexes, there are lots of electronic configurations with very similar energies and the mixing among these configurations are very strong. In such cases, multi-configurational based method

is required to describe the electronic structure. To describe this strong correlation, one has to incorporate these important configurations in the reference space. The CASSCF method accounts for the most important configurations by introducing a set of orbitals, and then all possible configurations within the active space are produced. The orbitals included in the active space are called active orbitals, and they can be doubly occupied, singly occupied or empty. These orbitals are optimized through all possible rotations between the active orbitals and inactive orbitals, active orbitals and secondary orbitals, as well as inactive orbitals and secondary orbitals. The computation of CASSCF becomes demanding with the increase of the number of active orbitals, especially when the number of active orbitals is close to the number of electrons. To reduce the computational cost, the active space can be partitioned into subspaces, namely a restricted active space SCF (RASSCF) method.[58] In this method, the excitation level is usually limited to one or two electrons, hence give a limited number of excited configurations.

3.3.1 Second-order perturbation

The CAASCF/RASSCF method can describe correlation well within the chosen reference space, however, remaining correlation called dynamic correlation is still neglected. The dynamical correlation can be treated perturbatively using CASPT2,[62–64] which uses a CASSCF reference wavefunction. For some cases where several states have strong mixing, the CASSCF wavefunction is not good reference state for the perturbation calculation, to solve this problem, the CASPT2 calculations can be performed as multi-state (MS)-CASPT2.[65]

The small difference between \hat{H} and \hat{H}_0 is seen merely as 'perturbation', and all quantities of the system described by \hat{H} (the perturbed system) can be expanded as a Taylor series starting from the unperturbed quantities (those of \hat{H}_0). The expansion can be solved in terms of a parameter γ :

$$\hat{H}(\mathbf{r}, \mathbf{R}) = \hat{H}^{(0)}(\mathbf{r}, \mathbf{R}) + \gamma \hat{H}^{(1)}(\mathbf{r}, \mathbf{R}) + \gamma^2 \hat{H}^{(2)}(\mathbf{r}, \mathbf{R}) + \dots \quad (3.22)$$

the wavefunction can be written as:

$$\Psi_n(\mathbf{r}, \mathbf{R}) = \Psi_n^{(0)}(\mathbf{r}, \mathbf{R}) + \gamma \Psi_n^{(1)}(\mathbf{r}, \mathbf{R}) + \gamma^2 \Psi_n^{(2)}(\mathbf{r}, \mathbf{R}) + \dots \quad (3.23)$$

and the energy can be written as:

$$E_n(\mathbf{r}, \mathbf{R}) = E_n^{(0)}(\mathbf{r}, \mathbf{R}) + \gamma E_n^{(1)}(\mathbf{r}, \mathbf{R}) + \gamma^2 E_n^{(2)}(\mathbf{r}, \mathbf{R}) + \dots \quad (3.24)$$

The Ψ_n^1 and E_n^1 are the first order corrections to the wavefunction and energy respectively. Ψ_n^2 and E_n^2 are the second order corrections and so on. The task of perturbation theory is to approximate the energies and wavefunctions of the perturbed system by calculating corrections up to a given order. In many

textbooks the expansion of the Hamiltonian is terminated after the first order term, i.e. $\hat{H}(\mathbf{r}, \mathbf{R}) = \hat{H}^{(0)}(\mathbf{r}, \mathbf{R}) + \gamma\hat{H}^{(1)}(\mathbf{r}, \mathbf{R})$, as this is sufficient for many physical problems.

The chain equation can be obtained as the solution is independent on the γ :

$$\hat{H}^{(0)}(\mathbf{r}, \mathbf{R})\Psi_n^{(0)}(\mathbf{r}, \mathbf{R}) = E_n^{(0)}(\mathbf{r}, \mathbf{R})\Psi_n^{(0)}(\mathbf{r}, \mathbf{R}) \quad (3.25)$$

$$(\hat{H}^{(0)}(\mathbf{r}, \mathbf{R}) - E_n^{(0)}(\mathbf{r}, \mathbf{R}))\Psi_n^{(1)}(\mathbf{r}, \mathbf{R}) = (E_n^{(1)}(\mathbf{r}, \mathbf{R}) - \hat{H}^{(1)}(\mathbf{r}, \mathbf{R}))\Psi_n^{(0)}(\mathbf{r}, \mathbf{R}) \quad (3.26)$$

$$\begin{aligned} (\hat{H}^{(0)}(\mathbf{r}, \mathbf{R}) - E_n^{(0)}(\mathbf{r}, \mathbf{R}))\Psi_n^{(2)}(\mathbf{r}, \mathbf{R}) &= (E_n^{(2)}(\mathbf{r}, \mathbf{R}) - \hat{H}^{(2)}(\mathbf{r}, \mathbf{R}))\Psi_n^{(0)}(\mathbf{r}, \mathbf{R}) \\ &+ (E_n^{(1)}(\mathbf{r}, \mathbf{R}) - \hat{H}^{(1)}(\mathbf{r}, \mathbf{R}))\Psi_n^{(1)}(\mathbf{r}, \mathbf{R}) \end{aligned} \quad (3.27)$$

To simplify the expansion from now on we will use bra-ket notation, representing wavefunction corrections by their state number, so $\Psi_n^{(0)}(\mathbf{r}, \mathbf{R}) \equiv |n^{(0)}\rangle$, $\Psi_n^{(1)}(\mathbf{r}, \mathbf{R}) \equiv |n^{(1)}\rangle$, etc.

Take Eq. (3.26) in ket notation, we can derive an expression for calculating the first order correction to the energy $E^{(1)}$:

$$(\hat{H}^{(0)}(\mathbf{r}, \mathbf{R}) - E_n^{(0)}(\mathbf{r}, \mathbf{R}))|n^{(1)}\rangle = (E_n^{(1)}(\mathbf{r}, \mathbf{R}) - \hat{H}^{(1)}(\mathbf{r}, \mathbf{R}))|n^{(0)}\rangle \quad (3.28)$$

and multiply from the left by $|n^{(0)}\rangle$ to obtain:

$$\langle n^{(0)} | (\hat{H}^{(0)}(\mathbf{r}, \mathbf{R}) - E_n^{(0)}(\mathbf{r}, \mathbf{R})) | n^{(1)} \rangle = \langle n^{(0)} | (E_n^{(1)}(\mathbf{r}, \mathbf{R}) - \hat{H}^{(1)}(\mathbf{r}, \mathbf{R})) | n^{(0)} \rangle \quad (3.29)$$

In the end, we can get the first order correction to the energy:

$$E_n^{(1)}(\mathbf{r}, \mathbf{R}) = \langle n^{(0)} | \hat{H}^{(1)}(\mathbf{r}, \mathbf{R}) | n^{(0)} \rangle \quad (3.30)$$

Similarly, we can derive an expression for calculating the second order correction to the energy $E^{(2)}$ by applying $\langle n^{(0)} |$ from the left to Eq. (3.27),

$$\begin{aligned} E_n^{(2)}(\mathbf{r}, \mathbf{R}) &= \langle n^{(0)} | \hat{H}^{(2)}(\mathbf{r}, \mathbf{R}) | n^{(0)} \rangle + \langle n^{(0)} | \hat{H}^{(1)}(\mathbf{r}, \mathbf{R}) | n^{(1)} \rangle \\ &= H_{nn}^{(2)}(\mathbf{r}, \mathbf{R}) + \langle n^{(0)} | \hat{H}^{(1)}(\mathbf{r}, \mathbf{R}) | n^{(1)} \rangle \end{aligned} \quad (3.31)$$

Finally, the second-order correction energy can be represented as:

$$E_{(2)}(\mathbf{r}, \mathbf{R}) = H_{nn}^{(2)}(\mathbf{r}, \mathbf{R}) + \sum_{n \neq k} \frac{H_{nk}^1(\mathbf{r}, \mathbf{R}) + H_{kn}^1(\mathbf{r}, \mathbf{R})}{E_n^0(\mathbf{r}, \mathbf{R}) - E_k^{0s}(\mathbf{r}, \mathbf{R})} \quad (3.32)$$

By including the dynamic correlations, we could expect the CASPT2 would give state a improved description of energy compared to CASSCF state. Through the MS-CASPT2 calculations, the strong interactions between states in same symmetry can be well described, which might be important to describe the charge transfer features in the X-ray spectra.

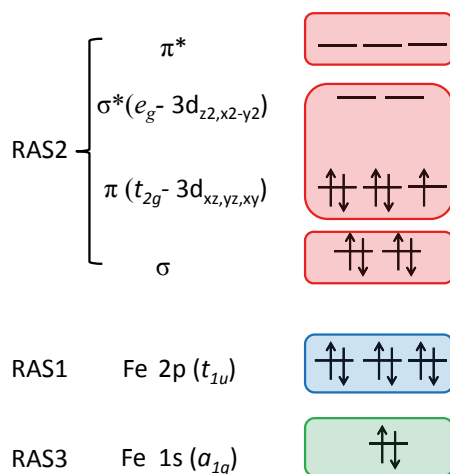


Figure 3.1. The active space for $[Fe(CN)_6]^{3-}$. 1s or 2p orbitals can be included in either RAS1 or RAS3. Important metal 3d orbitals are included as well as important correlating ligand character orbitals are included in RAS2. Labels appropriate for O_h symmetry is used.

3.3.2 RAS method for X-ray spectra

Computations of excited states in the X-ray processes are implemented using state average RASSCF.[66] It has been used to model valence excitation and core-hole excitation by choosing the most important orbitals in the active space, not only the metal character 3d molecular orbitals, but also the important ligand character molecular orbitals, as indicated in Figure 3.1. It allows for a full configuration interaction among the active orbitals. The full configuration interaction in the active space not only makes sure that the correct final states are spanned, but also takes care of the correlation among the active electrons.

Scalar relativistic effects have been included by using a Douglas-Kroll Hamiltonian [67] in combination with a relativistic atomic natural orbital basis set.[68, 69]

SOC is calculated from a one-electron spin-orbit Hamiltonian based on atomic mean field integrals.[66, 70] The SOC free eigenstates are used as a basis for computing SOC matrix elements, and the spin-orbit eigenstates are then obtained by diagonalizing the SOC matrix, giving SOC states $|\xi\rangle$, which are linear combinations of SOC free states $|\eta\rangle$:

$$|\xi\rangle = \sum_{\eta} c_{\eta}^{\xi} |\eta\rangle \quad (3.33)$$

The weight (ω) from each SOC free state can be acquired from the square of the coefficient ($c_{\vec{\eta}}^{\xi}$)². These eigenstates are then utilized to calculate the strength of the transitions using the restricted active space state interaction (RASSI) approach.[66, 70] The corresponding equation for the 1st order cartesian multipole moments (dipole transition moment operator, $\vec{\mu}_{\sigma\delta}$) is:

$$f_{(\sigma\rightarrow\delta)}^D = \frac{2m_e}{3\hbar^2 e^2} \Delta E_{\sigma\delta} |\vec{\mu}_{\sigma\delta}|^2 \quad (3.34)$$

Intensities for quadrupole transitions have been calculated using an implementation of the so-called origin independent quadrupole intensities, where all terms in the second-order expansion in the intensities are calculated, and not only the terms from the zeroth and first order of the wave-vector expansion.[71] The isotropically averaged quadrupole transition intensity ($f_{(\sigma\rightarrow\delta)}^Q$) of the 1s to 3d transition consists of electric quadrupole electric quadrupole contribution f^{qq} , magnetic dipole magnetic dipole contribution f^{mm} , the electric quadrupole magnetic dipole contribution f^{qm} , electric dipole electric octupole contribution $f^{\mu o}$, and electric dipole magnetic quadrupole contribution $f^{\mu\bar{m}}$. [71]

$$f_{(\sigma\rightarrow\delta)}^Q = \frac{m_e}{20\hbar^4 e^2 c^2} \Delta E_{\sigma\delta}^3 [|\vec{T}_{\sigma\delta}^q|^2 + |\vec{T}_{\sigma\delta}^m|^2 + 2\text{Re}(T_{\sigma\delta}^{q,*} T_{\sigma\delta}^m) + 2\text{Re}(T_{\sigma\delta}^{\mu,*} T_{\sigma\delta}^o) + 2\text{Re}(T_{\sigma\delta}^{\mu,*} T_{\sigma\delta}^{\bar{m}})] \quad (3.35)$$

and can be simplified as

$$f_{(\sigma\rightarrow\delta)}^Q = f_{(\sigma\rightarrow\delta)}^{qq} + f_{(\sigma\rightarrow\delta)}^{mm} + f_{(\sigma\rightarrow\delta)}^{qm} + f_{(\sigma\rightarrow\delta)}^{\mu o} + f_{(\sigma\rightarrow\delta)}^{\mu\bar{m}} \quad (3.36)$$

where m_e and e are the mass and charge of the electron, respectively, \hbar is reduced Planck constant, c is the speed of light in atomic units, $\Delta E_{\sigma\delta}$ is the transition energy, and T is transition moment. The RIXS calculation is theoretically described by the Kramers-Heisenberg formula[72]:

$$F(\Omega, \omega) = \sum_f \left| \sum_n \frac{\langle f | T_e | i \rangle \langle i | T_a | g \rangle}{K(\Gamma_i)} \right|^2 \times K(\Gamma_f) \quad (3.37)$$

where the scattering intensity F is a function of incident energy (Ω) and emitted X-ray energy (ω), the $|g\rangle$, $|i\rangle$, and $|f\rangle$ are ground, intermediate and final states respectively. T_a and T_e are transition operators for the absorption and emission processes respectively. $K(\Gamma)$ depends on the resonance energy and the lifetime broadening Γ of each state.

3.4 Charge transfer multiplet model

One possibility to properly account for the multiplet effects is to use the semi-empirical charge-transfer multiplet (CTM) model.[73, 74] This method includes all relevant final states and gives a balanced description of electron

repulsion and SOC. For a free atom without any influence from the surroundings, the Hamiltonian for an N-electron atom can be written as:

$$H = \sum_N \frac{P_i^2}{2m} + \sum_N \frac{-Ze^2}{r_i} + \sum_N \vartheta(r_i) l_i \cdot s_i + \sum_{\text{pairs}} \frac{e^2}{r_{ij}} \quad (3.38)$$

where the first term denotes the kinetic energy of electrons, the second term denotes the electrostatic interaction of electrons with the nucleus, the third term denotes the SOC, and the last term denotes electron-electron repulsion. In a given configuration, the first two terms in the Hamiltonian represent the average energy of the configuration and have no contribution to the multiplet splitting. The last two terms represent the relative energy of the different terms within configurations and have contribution to the multiplet splitting. The ligand field is treated as a perturbation to the free atomic case and is introduced by adding a new term in the atomic Hamiltonian.

For the highly covalent molecular systems, the charge transfer features are included by configuration interactions between the ground state (d^n) and introduced extra LMCT configuration ($d^{n+1}\underline{L}$), and MLCT configurations ($d^{n-1}L^-$). The CTM model often achieves excellent agreement with experimental data for highly symmetric systems through a multi-parameter fit to the electron-electron interaction, the ligand field, and the charge transfer states.[42] However, the number of parameters used to describe the effects of the ligand environment increases with decreasing symmetry, which makes it difficult to describe complexes with low or no symmetry. Moreover, when both dipole and quadrupole transitions have to be accounted for, additional parameters describing the amount of mixing are required. This further makes it less straightforward to apply and analyze the results of the CTM method for low-symmetry complexes.

3.5 Other methods for modelling X-ray spectra

X-ray spectra that involve core holes can be described by a number of different approaches, *e.g.* multiple scattering,[75, 76], static exchange,[77] transition-potential density-functional theory (DFT),[78] Bethe-Salpeter approach,[79, 80] and complex polarization propagator methods.[81] Recently, time dependent (TD) DFT method has been used to predict and interpret XAS.[82–85] This provides a framework to calculate transition energies and intensities with favourable balance between accuracy and computational time. A limitation of many of these approaches, is that they do not incorporate the necessary physics to correctly account for the multiplet effects arising from electron–electron correlations. A DFT restricted-open shell configuration interaction with singles (DFT/ROCIS) approach was developed to cover all the multiplets that arise from the atomic terms.[86–89] In this method, the ground state and a

number of excited states of the non-relativistic Hamiltonian are firstly calculated. For a ground state with total spin S , excitation to a number of excited states with total spin $S' = S, S - 1$, and $S + 1$ are calculated. The lack of doubly occupied orbitals in the DFT/ROCIS will exclude excitations from the core orbitals combined with simultaneous excitations from doubly occupied valence orbitals into empty or singly occupied valence orbitals, e.g., the shake-up transition of LMCT type. Moreover, due to its single reference character, DFT/ROCIS is not applicable to molecules with an orbitally degenerate ground state. The DFT/ROCIS account for dynamic correction by using DFT orbitals with specified empirical parameter, but it should be stressed that the DFT orbitals can yield improved results for covalent bonding, which make it very useful on highly covalent transition metal complexes.

4. Soft X-rays

In this chapter, selected results from the RAS simulations (papers I to IV) of metal L-edge XAS are presented. The RAS method is firstly used to simulate the atomic Fe^{3+} with charges mimic the strong ligand field, then it is extended to calculate the metal L-edge XAS of low spin complexes $[Fe(CN)_6]^n$ (paper I and II) and $[Fe(P)(ImH)_2]^n$ (paper III) (P = porphyrin, ImH = imidazole) in ferrous and ferric oxidation state. Then the RAS calculations on $[Fe(P)]$ system have been performed to fingerprint the electronic states. In the last section, the two-photon process 3d-PFY-XAS as a probe of electronic structure of manganese complexes in solution are simulated and discussed (paper IV).

4.1 Atomic calculation of low-spin Fe^{3+}

The RAS and semi-empirical CTM model L-edge XAS of the Fe^{3+} in a strong field are displayed in Figure 4.1. Ferric systems with a strong field have a low-spin ${}^2T_{2g}$ ($2p^6t_{2g}^5e_g^0$) ground state. The calculated RAS spectra overlap well with the CTM model results.

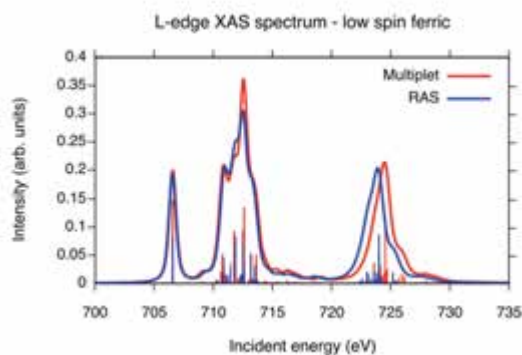


Figure 4.1. L-edge XAS spectra of the Fe^{3+} ion, with strong ligand-field splitting using RAS (blue) and the CTM model (red).

To understand the role of SOC from $2p$ and $3d$ orbitals, and the multiplet effects on the L-edge spectral features, the spectrum of low-spin Fe^{3+} ion was analysed in detail, see Figure 4.2. Without SOC, there is only one edge, split by ligand field and multiplet effects. The spectrum is split into into L_3 ($J = \frac{3}{2}$)

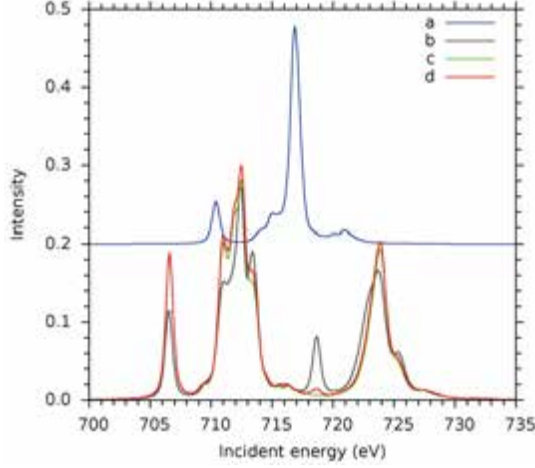


Figure 4.2. RAS L-edge XAS spectra of the Fe^{3+} ion with different treatments of $2p$ and $3d$ SOC. (a) Spectrum calculated without SOC. (b) Spectrum with $2p$ SOC but using one of the ${}^2T_{2g}$ ground states, i.e., without considering splitting from $3d$ SOC. (c) Spectrum calculated from the Γ_7^+ ($J=\frac{1}{2}$) $3d$ SOC ground states. (d) Spectrum calculated from a Boltzmann distribution of Γ_7^+ ($J=\frac{1}{2}$) and Γ_8^+ ($J=\frac{3}{2}$) states.

and L_2 ($J = \frac{1}{2}$) edges by including $2p$ SOC, and the mixing of states with different multiplicity can further change the spectral features.

The $3d$ SOC constant (0.05 eV) is much weaker compared to the $2p$ one (8 eV), but still has important effects on the spectra. Without $3d$ SOC, the ground state is six-fold degenerate stems from a three-fold orbital degeneracy and a doublet spin multiplicity. $3d$ SOC splits these six states into doubly-degenerate $J=\frac{1}{2}$, Γ_7^+ in Bethe double-group notation, and four-fold degenerate Γ_8^+ ($J = \frac{3}{2}$) states, with the Γ_7^+ states lower in energy by 0.086 eV, see Figure 4.3.

The changes in spectral shape are connected to differences in selection rules for the different SOC states where e.g., transitions to the L_2 t_{2g} peak (Γ_6^-) are electric dipole forbidden. $3d$ SOC also leads to changes in the broad $2p \rightarrow e_g$ resonance, partly because there are Γ_6^- states also in this region, and partly because the change in ground state leads to differences in the intensity mechanisms.[50] This example shows how a correct description of the multi-reference character of the degenerate ground state, together with an accurate description of $3d$ SOC, is required for the modeling of L-edge XAS spectra. A further improvement is to allow for a Boltzmann population of the different initial states. However, with a splitting of 0.086 eV only a minor fraction (3.5%) populates the Γ_8^+ states at room temperature and the effect on the calculated spectrum is relatively small, see Figure 4.2. The intensities of transitions arising from Γ_8^+ state will significantly depend on the temperature, since the state will be more populated at higher temperature.

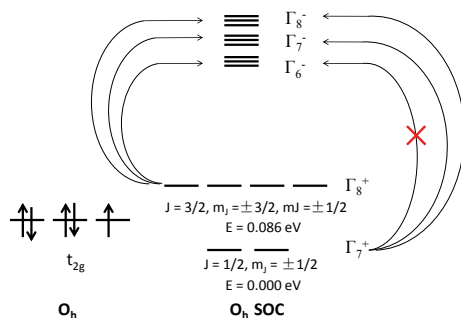


Figure 4.3. Energy levels of the SOC ground states with configuration ${}^2T_{2g}$ $2p^6(t_{2g})^5(e_g)^0$ for the low-spin Fe^{3+} ion. The selection rule of transition is indicated with arrows, the forbidden transition from Γ_7^+ ground state to Γ_6^- excited state is marked with a cross.

4.2 Metal L-edge XAS of low-spin iron complexes

$[Fe(CN)_6]^n$ and $[Fe(P)(ImH)_2]^n$ are low spin systems, but with different ligand environment. The CN ligands of $[Fe(CN)_6]^n$ give O_h and D_{4h} symmetry for ferrous and ferric oxidation state respectively. The CN^- can interact with $d_{x^2-y^2}$ and d_{z^2} as σ donors, and interact with d_{xy}, d_{xz}, d_{yz} as π acceptor forming back-donation orbitals, see paper I. The ligand set of $[Fe(P)(ImH)_2]^n$ is consist of porphyrin (P) and axial imidazoles (ImH). The symmetry of heme complex is C_{2h} . Both porphyrin and imidazoles ligands can act as σ and π donors, and π acceptors interacting with metal 3d orbitals. The active space of low spin ferrous iron complex is presented in Figure 4.4.

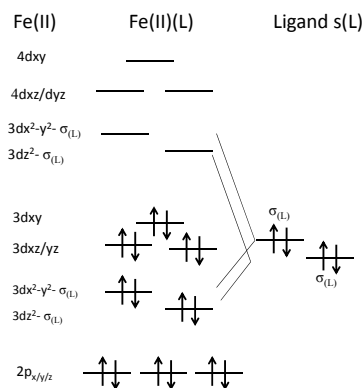


Figure 4.4. The active spaces for low spin ferrous iron complex (one electron less for ferric oxidation).

4.2.1 Fingerprint the oxidation states

The $[Fe(CN)_6]^n$ complexes are adopted as σ donor and π back-donation prototypical models. The experimental L_3 edge XAS of $[Fe(CN)_6]^{4-}$ has two intense peaks at 709.1 and 710.7 eV,[41] which can be assigned as e_g and back-donation π^* character peak respectively. The same two peaks appear also in the L_2 edge but with smaller intensities, see the blue curve Figure 4.5a. The experimental L-edge XAS of $[Fe(CN)_6]^{3-}$ has three distinct peaks at the L_3 edge, located at 705.8 eV, 710.1 eV and 712.4 eV, which can be assigned to t_{2g} , e_g and anti-bonding (π^*) character peak respectively, see Figure 4.5a. There are two peaks in the L_2 edge, the main peak at 722.8 eV and a minor peak at 726 eV.[41] Compared to XAS L-edge XAS of $[Fe(CN)_6]^{4-}$, one evident difference is the peak at 705.8 eV, due to a singly occupied t_{2g} character orbitals in $[Fe(CN)_6]^{3-}$. Another difference is the e_g peak of $[Fe(CN)_6]^{4-}$ shifts to higher energy by ~ 1.0 eV, and the π^* peak shifts by ~ 1.7 eV due to the oxidation state change, see Figure 4.5a.

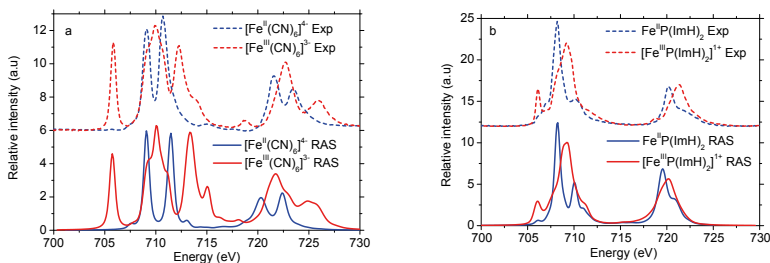


Figure 4.5. Metal L-edge XAS of low spin $[Fe(CN)_6]^{n-}$ (left) and $[Fe(P)(ImH)_2]^n$ (right) in ferrous (blue) and ferric (red) oxidation state. (number of final states for each spin: $[Fe(CN)_6]^{3-}$ (120), $[Fe(CN)_6]^{4-}$ (60), $[Fe(P)(ImH)_2]$ (120), $[Fe(P)(ImH)_2]^{1+}$ (60)).

The RAS active space included two ligand-dominated filled σ orbitals, three empty ligand-centered anti-bonding (π^*) orbitals and five metal $3d$ character orbitals. The RAS calculations capture all the important spectral features of the experimental spectra, see Figure 4.5a. The RAS calculation of $[Fe(CN)_6]^{4-}$ underestimated the intensity of the π^* peak at the L_3 edge, and the energy of the third peak at the L_3 edge by ~ 0.8 eV. While the energy of L_2 edge was underestimated by ~ 1.0 eV. This is due to an error in the calculation of the strength of the $2p$ SOC. The calculation of $[Fe(CN)_6]^{3-}$ gave a slightly overestimated intensity of the π^* peak, and the energy is shifted by ~ 1.0 eV.

The spectral features of $[Fe(P)(ImH)_2]^n$ are similar to the $[Fe(CN)_6]^n$ but lack the intense π^* peak, which will be analyzed in the following section.

4.2.2 Fingerprint the ligand environment

For systems with same oxidation state, one major difference is the intensity of back-donation π^* peak. In metal L edge XAS of $[Fe(P)(ImH)_2]^n$ complex, the spectra do not show the pronounced π^* peak, see Figure 4.5b, because the heme ligand does not act as a particularly good π acceptor, which results in a rather limited metal character in the π^* orbitals.[90] The very limited π back-bonding in this complex has been suggested from NMR spectroscopy results and orbital covalency calculation using the CTM model.[90, 91] In $[Fe(CN)_6]^n$, the intense π^* peak has been interpreted as intensity borrowing from e_g excitation, see ref [41] and paper 1. The orbital contribution to the metal L edge XAS has also confirmed the intensity mechanism to the π^* peak, see the example of $[Fe(CN)_6]^{3-}$ in Figure 4.6. From the orbital contribution analysis, we can see the first peak at 705.8 eV can be assigned to a $2p \rightarrow t_{2g}$ transition. The second peak at 710 eV is mainly from $2p \rightarrow e_g$ excitations. The third peak at around 713.4 eV is from $2p \rightarrow \pi^*$ transitions together with $t_{2g} \rightarrow e_g$ excitations. The contributions for L_2 edge are mainly from the $2p \rightarrow e_g$ excitations, with very small $2p \rightarrow \pi^*$ transitions. The analysis of the X-ray spectra in terms of molecular orbital contributions enables a direct connection between a spectrum and the electronic structure features.

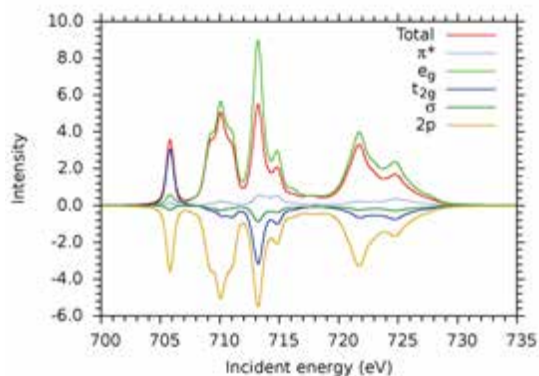


Figure 4.6. Orbital contribution analysis to the RAS calculated metal L edge XAS of $[Fe(CN)_6]^{3-}$.

4.2.3 Fingerprint the different electronic states

Ferrous and ferric $[Fe(P)(ImH)_2]^n$ have well-defined low-spin electronic ground states and the simulations have reproduced all spectral features with good accuracy. In this section, the RAS method is used to test the ability to distinguish between different electronic states. Spectra have been simulated for four different low-lying electronic states of $Fe^{II}(P)$ ($^3A_{2g}$, $^5A_{1g}$, 3E_g and 5E_g), the active space is presented in Figure 4.7 which have then been ranked based on

the similarity to experiment as judged by the cosine similarity (CS). The possibility to use spectral fingerprints to confidently identify an unknown species is discussed.

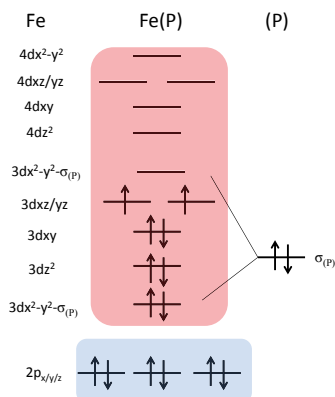


Figure 4.7. The active spaces for $Fe^{II}(P)$.

Previous theoretical calculations have indicated that there are several low-lying electronic states of $Fe^{II}(P)$ of different multiplicity, see Figure 4.8, and the energies of different spin states have been varied among different theories.[92–96] The latest CASPT2 calculations predicted the lowest state to be ${}^5A_{1g}$ instead of the correct ${}^3A_{2g}$, which is in line with observations that CASPT2 systematically overstabilizes high spin with respect to lower spin states.[94] Therefore, it is interesting to see how RAS X-ray spectra simulations to fingerprint different electronic states of the same complex.

The experimental spectrum has a broad L_3 edge,[97] with peaks at 705.7, 706.5 and a main peak at 708.1 eV, see black curve in Figure 4.9. There are also shoulders both on the low and high-energy side of L_3 edge. The broad L_3 edge reflects the multiplet structures available when there are several unpaired electrons already in the ground state. The L_2 edge is also rather broad with a maximum at ~ 720.5 eV.

The metal L edge spectra simulated using four different initial states, representing the pure electronic states ${}^3A_{2g}$, ${}^5A_{1g}$, 3E_g and 5E_g , are all rather different in shape, see Figure 4.9. The highest similarity is found for the correct ${}^3A_{2g}$ state. Looking at the simulated spectra, the triplets and quintets generally over- and underestimate intensities in different areas of the spectrum. It is therefore conceivable that a combination of the ${}^3A_{2g}$ with quintet could lead to better agreement with experiment. With increasing weight of the quintets, the low-energy region increases in intensity, as well as the main peak at 708.1 eV. At the same time, the L_2 edge decreases in intensity, better matching the experimental intensity. Plotting the similarity as a function the relative weight of the two states shows a maximum of 0.991 at 79% ${}^3A_{2g}$ + 21% ${}^5A_{1g}$, 0.992 at 83% ${}^3A_{2g}$ + 17% 5E_g , see Figure 4.10. With the aid of similarity analysis, the

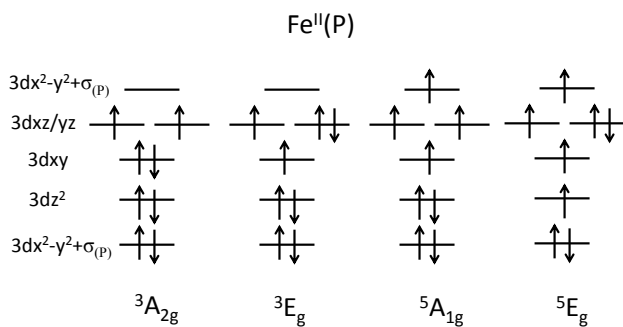


Figure 4.8. The electron configuration representations for low lying states of $\text{Fe}^{II}(\text{P})$.

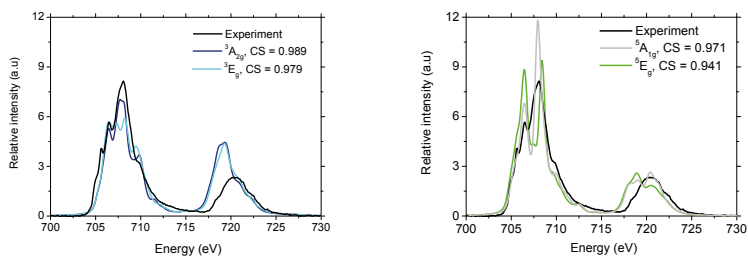


Figure 4.9. The experimental spectrum and RASPT2 calculated spectra of $\text{Fe}^{II}(\text{P})$ of different low-lying state.

RAS calculations including contribution from low lying states are performed. The higher CS scores are given in the calculations, which indicate improved simulated spectra are presented, see Figure 4.10.

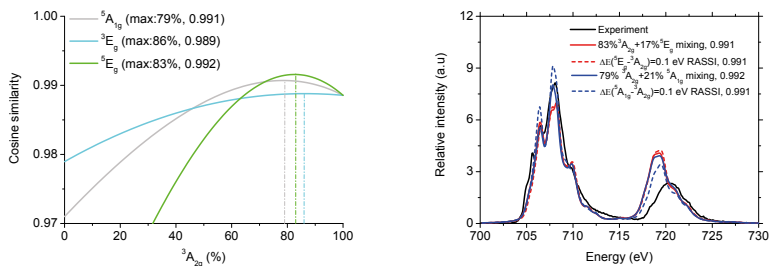


Figure 4.10. (Left) The CS along the mixing between low-lying states with ${}^3A_{2g}$. (Right) The comparison of corresponding linear mixing spectra with the RASPT2 calculated spectra giving similar percentage of different states.

4.2.4 Cost and stability of RAS method

The examples we adopted here range from small size ($[Fe(CN)_6]^n$) (Paper I and II) to medium size ($[Fe(P)(ImH)_2]^n$) (Paper III). Regarding the limitation of the molecule size, one possibility is to ignore the dynamical correlation added in the RASPT2 step and rely on the RASSCF results. The RASPT2 is a time consuming step, see Figure 4.11, and the RASSCF is eligible to provide qualitatively good results.[25, 26, 98, 99] One way to minimize the cost of the RASPT2 calculation is to do state specific (SS) RASPT2 instead of doing multi-state (MS)RASPT2, the SS-RASPT2 has relative lower computational cost and good accuracy in cases where no states interact strongly in the same symmetry.[65] Another alternative is to use smaller basis set, which would lead to an decrease in the number of basis functions. The triple-zeta basis set was adopted in this thesis for spectra calculations of small-size molecules. For medium-sized complexes, a double-zeta basis can give good results, e.g., the metal L-edge XAS calculations for heme systems.

For the one photon process spectra simulations, the core orbitals uses one of three RAS sub-spaces, which leaves flexibility in the design of the valence orbitals in another two RAS sub-spaces for lowering the computational cost for both RASSCF and RASPT2 step, see Figure 4.11.

4.2.5 Summary

The examples here showed the RAS can handle multiplet effects, 2p and 3d SOC, effects of both ligand donor bonding (LMCT) and back-donation (MLCT) and spectral features arising from multiple excitations. Through the

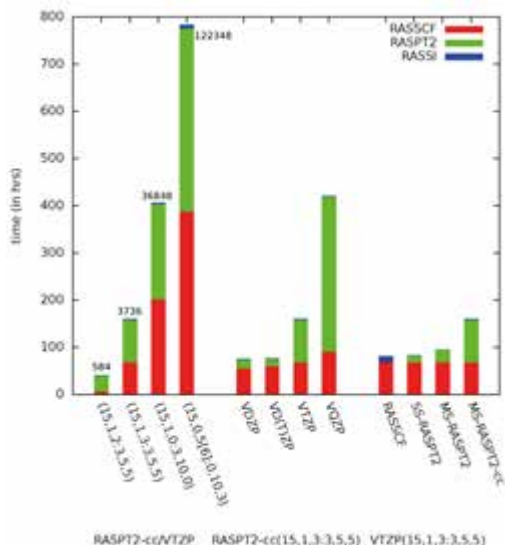


Figure 4.11. Analysis of the total computational cost for the various steps in the calculation the L-edge XAS spectra of $[FeCN_6]^{3-}$ as function of active space, basis set, and computational algorithm. The timings refer to an Intel Xeon E5-2660 "Sandy Bridge" processor at 2.2 GHz using 8 GB RAM. The numbers of doublet configuration state functions in B_{1g} symmetry are also shown for comparison.

comparison of metal L edge XAS of $[Fe(CN)_6]^n$ and $[Fe(P)(ImH)_2]^n$ in ferrous and ferric oxidation, the RAS simulations together with orbital contributions can be used to distinguish different oxidation state and ligand environment based on their spectral fingerprints. The understanding of the orbital interaction between metal and ligands has important implications for knowledge of the reactivity of catalyst centers in reaction, e.g, the heme center in biology. Through the metal L edge XAS calculation of $Fe^{II}(P)$ with different low-lying spin states, the accuracy gives us confidence to use RAS simulations to distinguish between different spin states based on their spectral fingerprints. The CS analysis is introduced to aid a quantitative measure of the similarity between calculated and experimental spectra. The applications here also show that RAS can be extended from small to medium size of systems by the proper selection of active space, basis set and computational algorithms.

4.3 PFY-XAS of manganese complexes

In the Mn_4CaO_5 cluster of the catalytic site of water oxidation in the oxygen-evolving complex (OEC) in the photosystem II protein complex, two H_2O molecules are oxidized and molecular O_2 is released. Tracking the electronic structure of the catalytic site of the metalloproteins in the time course of their biological reaction would largely benefit the artificial photosynthesis research.

In this section, the PFY-XAS of two prototypical models ($Mn^{II}(acac)_2$ and $Mn^{III}(acac)_3$) with different oxidation states are experimentally measured in solution. Radiation-damage free spectra are obtained using a reflective zone plate spectrometer for PFY detection.[20] In combination with RAS calculations, the electronic structure details such as spin density, charge density, and oxidation states are discussed. The efforts here pave the route to an interpretation of the spectra obtained from the protein sample.

4.3.1 PFY-XAS of $Mn^{II}(acac)_2$ and $Mn^{III}(acac)_3$

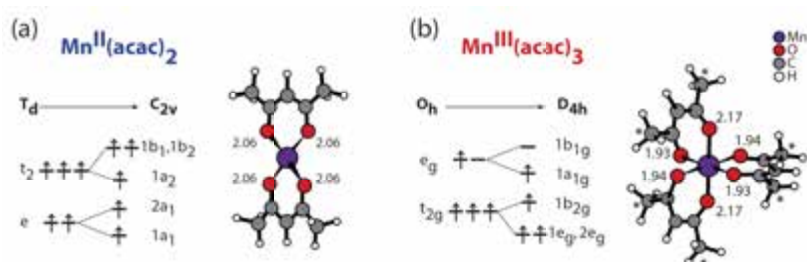


Figure 4.12. Schematic molecular orbital diagrams, structures of $Mn^{II}(acac)_2$ (a) and $Mn^{III}(acac)_3$ (b), (Mn-O bond lengths in Å). * in (b) mark methyl groups that were replaced with H in the RAS X-ray spectrum calculations.

The molecular orbital diagrams of the two Mn model complexes $Mn^{II}(acac)_2$ and $Mn^{III}(acac)_3$ are presented in Figure 4.12, these two complexes have different oxidation state, spin state and bonding environment. The full $Mn^{II}(acac)_2$ complex is formally treated in C_{2v} symmetry in the calculations, but the ligand environment is tetrahedral and T_d symmetry will be used in the discussion of electronic structure. The five metal $3d$ -dominated orbitals are all singly occupied which gives a e^2t^3 electron configuration with 6A_1 symmetry. The high-spin $Mn^{III}(acac)_3$ (5A symmetry with $t_2g^2e_g^2$) has four $3d$ electrons in an octahedral ligand field, which is Jahn-Teller unstable[100]. The complex has a D_{4h} ligand environment but the real symmetry is only C_2 .

The experimental L_3 edge of $Mn^{II}(acac)_2$ has a relatively narrow peak at ~ 639.6 eV, a clear spectral feature at ~ 641.0 eV, and another feature at ~ 643.5 eV. The L_2 edge is broad with a peak intensity at ~ 652.5 eV. The spectrum has similar features as those obtained from solid samples using a total electron yield (TEY) measurement [101]. The experimental L_3 edge of $Mn^{III}(acac)_3$ has a wide peak located at ~ 641.6 eV with a minor shoulder at ~ 640 eV. The L_2 edge has two peaks, located at ~ 651 eV and ~ 653 eV, respectively. One evident difference between $Mn^{II}(acac)_2$ and $Mn^{III}(acac)_3$ is the energy location of L_3 edge. The maximum peak of L_3 edge of $Mn^{III}(acac)_3$ locates ~ 2.0 eV higher than $Mn^{II}(acac)_2$, which can be a spectral fingerprint

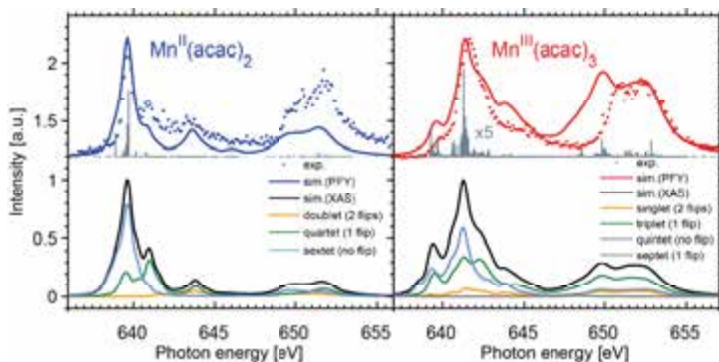


Figure 4.13. The experimental and RAS simulated PFY-XAS of $Mn^{II}(acac)_2$ (blue) and $Mn^{III}(acac)_3$ (red) (upper panel and the RAS transmission XAS together with spin contribution analysis of core excited states (bottom panel).

to the oxidation state. More details about the connection between energy shift and oxidation state will be discussed in the following sections.

The theoretical results are presented in Figure 4.13. The RAS calculated PFY-XAS of $Mn^{III}(acac)_3$ reproduce all the experimental features quite well, see Figure 4.13, but the splitting energy between the two peaks at the L_2 edge is slightly overestimated, which gives a two-peaks feature. The spin analysis of core excited states in the transmission XAS are presented below, the intensities of two spectra are dominated by the S (the same multiplicity as ground state), S-1 core excited states.

4.3.2 Spin and charge density

A common way to analyze the electron density from a quantum chemistry calculation is to assign charges and spins to individual atoms in the molecule. Here values of the LoProp charge[102] and Mulliken spin[103] analysis are reported. The assigned charges from RASSCF calculations for $Mn^{II}(acac)_2$ and $Mn^{III}(acac)_3$ are 1.56 and 2.08, see Table 4.1, while DFT (B3LYP)[104–107] calculations give 1.37 and 1.61. To isolate electronic structure changes from changes in the ligand environment, the artificial $[Mn^{II}(acac)_3]^{1-}$ complex has been analyzed. This model has similar charge, spin and spectrum as $Mn^{II}(acac)_2$ (spectrum is available in paper IV). The charges on the Mn centers do not match the oxidation states and the difference between the two complexes is not unity as expected from a one-electron oxidation.

For manganese systems the spin population is a better probe of the oxidation state[100]. $Mn^{II}(acac)_2$ has five unpaired electrons, while the corresponding number for $Mn^{III}(acac)_3$ is four. The Mulliken spin populations are relatively close to these values, 4.93 and 3.85 from RASSCF calculations, and DFT/B3LYP gives very similar numbers, 4.81 and 3.90 respectively.

	LoProp charge-B3LYP	Mulliken spin-B3LYP	LoProp charge-RASSCF	Mulliken spin-RASSCF
$Mn^{II}(acac)_2$	1.37	4.81	1.56	4.93
$[Mn^{II}(acac)_3]^{1-}$	1.37	4.82	1.52	4.92
$Mn^{III}(acac)_3$	1.61	3.90	2.08	3.85

Table 4.1. Charge and spin populations for the $Mn^{II}(acac)_2$, $[Mn^{II}(acac)_3]^{1-}$ and $Mn^{III}(acac)_3$ complexes.

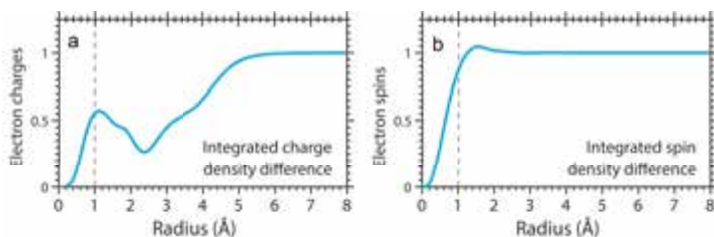


Figure 4.14. (a) Ground state integrated radial charge density (RCD) difference and (b) integrated Radial spin density (RSD) difference between $Mn^{III}(acac)_3$ and $[Mn^{II}(acac)_3]^{1-}$ ($[Mn^{II}(acac)_3]^{1-}$ minus $Mn^{III}(acac)_3$, in units of one electron charge/spin). All properties were extracted from RAS calculations and are plotted versus the radius R of a sphere around Mn. The dashed vertical lines indicate half the Mn-O bond length.

To understand the different behavior of the charge and spin assignments, the difference in radial charge density (RCD) when an electron is added to the system has been analyzed,[108] see Figure 4.14. It is clear that the additional charge (by adding one electron) is not localized at the metal center, but is rather delocalized over the entire complex due to local $3d - 3d$ Coulomb repulsion of the electrons in the Mn $3d$ -derived orbitals. In contrast, the change in radial spin density (RSD) is almost completed when reaching the first ligand shell due to the attractive exchange Coulomb interaction of parallel spins, see Figure 4.14. Upon addition of an electron, α and β electron densities thus rearrange differently in space. This spatial imbalance of α and β electron densities minimizes the overall the energy of the system resulting in charge scattered over the whole molecule and spin localized at the Mn.

The radial charge and density distribution analyses are performed on the core excited states, see Figure 4.15, to give a picture of the changes in electron density in the XAS process. Upon $2p$ to $3d$ excitation, very small RCD changes are visible above 0.6 \AA for both $Mn^{III}(acac)_3$ and $[Mn^{II}(acac)_3]^{1-}$ (Figure 4.15(a) and (b)). This suggests that $2p$ hole and $3d$ electron are strongly bound and that this effectively screens the valence electrons from the influence of the core hole. Figure 4.15(c and d) shows that spin density increases at the $2p$ shell while it decreases in the $3d$ shell, which reveals that the spin of the hole is preferentially aligned parallel with the majority spin of the $3d$ electrons. This is favorable due to the larger exchange energy between $2p$ and $3d$ electrons than the one between $3d$ and $3d$ electrons.

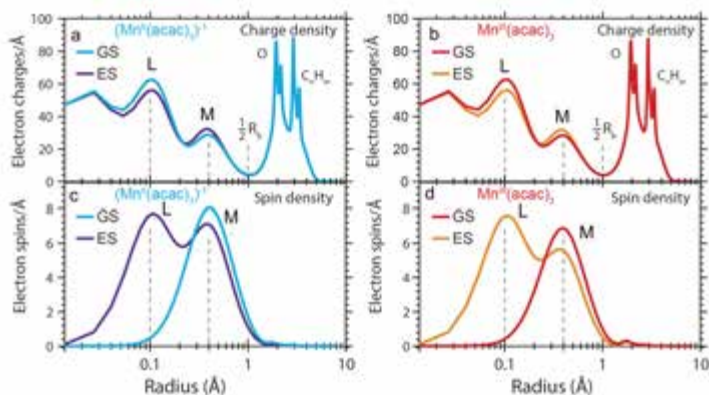


Figure 4.15. (a) RCD comparison of ground state and core excited state for $[\text{Mn}^{\text{II}}(\text{acac})_3]^{1-}$ and $\text{Mn}^{\text{III}}(\text{acac})_3$ (b). (c) RSD comparison of ground state and core excited state for $[\text{Mn}^{\text{II}}(\text{acac})_3]^{1-}$ and $\text{Mn}^{\text{III}}(\text{acac})_3$ (d).

4.3.3 Origin of the spectral shape and edge shift

From the analysis of spin contributions to the $\text{Mn}^{\text{III}}(\text{acac})_3$ spectrum in Figure 4.13, it is clear that both quintet and triplet final states give significant contributions to the spectrum. The large energy ranges for states with the same multiplicity are due to the different possibilities to couple 2p and 3d electrons to reach the same multiplicity. The significant overlap of quintet and triplet states leads to strong mixing through spin-orbit coupling. The spin-state splittings, and thus the shape of the spectrum are relatively well described in an atomic model. The reason for this is the localization of the spin density, which makes the molecule atomic-like when it comes to exchange interactions.

As the edge maxima of both Mn^{II} and Mn^{III} are dominated by states with the same multiplicity as the ground state, the energy shift is mainly due to differences in direct Coulomb interactions. Compared to atoms, it has been shown that these interactions are strongly reduced, at least in the solid state.[109, 110] This is connected to the delocalization of the electrons to minimize the $3d-3d$ Coulomb interaction, as shown by the RCD plot in Figure 4.14. However, even after taking delocalization into account, these interactions are still strong enough to lead to an observable shift in the L-edge XAS spectrum of high-spin manganese complexes.

4.3.4 Summary

We have presented the beam-damage-free PFY-XAS for two mono-manganese complexes $\text{Mn}^{\text{II}}(\text{acac})_2$ and $\text{Mn}^{\text{III}}(\text{acac})_3$ with different formal oxidation states. The RAS method well reproduced the experimental spectra features. Through the RCD and RSD analyses on both ground state and core excited states, we see that oxidation leads to local changes in spin on the metal, while charge is

redistributed over the entire molecule. The same picture holds for both ground and excited states. The spectral shape, which is strongly affected by the exchange interactions, reflects the local spin density. The shift in incident energy between two oxidation states is strongly affected by the direct Coulomb interactions. Although these interactions are screened due to the delocalization of charge, they are large enough to cause a visible shift in the edge energies.

5. Hard X-rays

The intensities and relative energies of metal K pre-edge features have high sensitivities to both geometric and electronic structure. Metal K pre-edge is in the hard X-ray regime and the absorption spectrum can be obtained *in situ*, which offer large freedom for probing samples. It can be used to probe dilute enzymatic systems and working catalysts.[36, 40] The K pre-edge features are not well resolved due to the short lifetime of the 1s core hole of the final states, which gives a relative larger bandwidth (~ 1.25 eV for Fe) than the metal L edge. The electronic structure details from the K pre-edge can be extracted either by the assistance of accurate theoretical calculations,(Papers V and VI) or by the use of RIXS. With the emergence of RIXS that can give high-resolution spectral information, it has become important to find a theoretical method that accurately simulates and interprets spectroscopy in the K edge. It requires a method can treat the different important effects that shape the spectral features: ligand-field splitting, multiplet structures, $3d-4p$ orbital hybridization, and charge-transfer transitions. The RAS application on 1s2p RIXS will be discussed in this thesis (Paper VII).

5.1 Metal K pre-edge XAS

Here the RAS method is introduced for the first time to calculate metal K pre-edge spectra of open-shell transition metal systems (papers V and VI). Intensities for quadrupole transitions have been calculated using an implementation of origin independent quadrupole intensities, where all terms in the second-order expansion in the intensities are calculated, and not only the terms from the zeroth and first order of the wave-vector expansion.[71] The performance of the RAS method is tested by applying it to six iron complexes; $[FeCl_6]^{n-}$, $[FeCl_4]^{n-}$, and $[Fe(CN)_6]^{n-}$ in ferrous and ferric oxidation states. The RAS calculations reproduces the spectral shape of all complexes with an average error for the peak splitting of only 0.1 eV, see Table 5.1. The accuracy with which both intensities and relative energies can be well reproduced, suggests that the RAS method can be used to identify and predict changes in metal K pre-edge spectra that comes from changes in both oxidation state and ligand environment. The results for complexes $[FeCl_6]^{4-}$, $[FeCl_4]^{2-}$, and $[Fe(CN)_6]^{3-}$ will be mainly discussed in this thesis, other K pre-edge spectra of mono-metal complexes and dimer are available in Paper V and VI.

Table 5.1. Energies (in eV) and fitted pre-edge areas from experiment and theory.

	Experiment ^a	RAS	CTM ^d	TD-DFT ^e
$[FeCl_6]^{3-}$				
E1(int)	7112.8(2.6)	-	-	-
E2(int)	7114.0(1.4)	7114.1	7114.0	7113.6
E3(int)	-	7118.3	7118.7	-
ratio ^b	3.7:2.0	3.5:2.0:0.7	3.4:2.0:0.4	-
$[FeCl_6]^{4-}$				
E1(int)	7111.3(1.2)	-	-	-
E2(int)	7111.8(1.8)	7111.9	7112.1	7112.3
E3(int)	7113.4(0.6)	7113.4	7113.5	-
ratio ^b	2.0:3.0:1.0	1.8:0.9:1.0	1.8:1.0:1.0	-
$[FeCl_4]^{1-}$				
E1(int)	7113.2(20.7)	-	-	7113.2
E2(int)	-	7116.6	-	-
D/Q ratio ^c	3.2:1.0	3.5:1.0	-	7.0:1.0
$[FeCl_4]^{2-}$				
E1(int)	7111.6(8.6)	-	-	-
E2(int)	7113.1(4.3)	7113.1	-	7112.3
D/Q ratio ^c	2.3:1.0	2.4:1.0	-	7.5:1.0
$[Fe(CN)_6]^{4-}$				
E1(int)	7112.9(4.2)	-	-	-
E2(int)	-	7115.6	7115.1	7113.5
ratio ^b	-	2.0:1.0	4.0:1.0	-
$[Fe(CN)_6]^{3-}$				
E1(int)	7110.1(1.0)	-	-	-
E2(int)	7113.3(4.1)	7113.3	7113.4	7113.6
E3(int)	-	7117.3	7117.1	7115.2
ratio ^b	1.0:4.1	1.0:4.2:1.6	1.0:4.4:0.2	-

^a Energies and fitted pre-edge areas (x100) from reference [42].

^b Intensity ratio between peaks.

^c Ratio between electric dipole (D) and electric quadrupole (Q) contributions.

^d CTM results.

^e TD-DFT results (BP86 functional) from reference [82].

5.1.1 Multiplet structures

The $[FeCl_6]^{4-}$ complex is adopted as σ and π donor prototypical model. The $[FeCl_6]^{4-}$ experimental spectrum appears to have two pre-edge peaks, but a closer analysis reveals two close-lying states (at 7111.3 and 7111.8 eV), followed by a third state at higher energy (7113.4 eV), see Figure 5.1 and Table 5.1.

For $[FeCl_6]^{4-}$, the ground state has an electronic configuration $t_{2g}^4 e_g^2$. After electron excitation from $1s$ to metal $3d$ character orbitals, the excited configuration $t_{2g}^5 e_g^2$ can only give a ${}^4T_{1g}$ symmetry state. The excited configuration $t_{2g}^4 e_g^3$ gives rise to ${}^4T_{1g}$ and ${}^4T_{2g}$ terms, which are split by $3d - 3d$ electron interactions, see Figure 5.1. The difference between the two e_g final

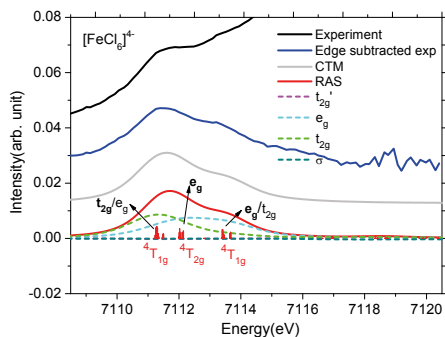


Figure 5.1. K pre-edge XAS of $[FeCl_6]^{4-}$. Experimental spectra (black), the edge-subtracted spectra (blue), CTM calculation spectra (light gray), RAS calculations spectra (red). The orbital contribution analyses are shown using dash lines, the main contributions are marked in bold. Contributions from 1s orbital are omitted.

states is most easily seen by considering a wavefunction where the spin-down t_{2g} electron is in the d_{xy} orbitals. In that case the ${}^4T_{2g}$ state has the spin-down e_g electron in the d_{z^2} orbital, while in the ${}^4T_{1g}$ state it is in the $d_{x^2-y^2}$ orbital. In the latter case, the two orbitals are in the same plane, leading to a larger electron-electron repulsion than if the orbitals are in different planes. The energy difference can be used as an indirect measure of orbital covalency, because higher covalency decreases the $d-d$ repulsion, and thus the energy difference between the two e_g states. However, this energy difference does not provide information about individual covalencies, only the combined effect of both e_g and t_{2g} .

The two ${}^4T_{1g}$ states can mix because they belong to the same irreducible representations, this is visible in the orbital contribution analysis where the two peaks include contributions from both t_{2g} and e_g orbitals, see Figure 5.1. The experimental splitting between the first ${}^4T_{1g}$ state and the ${}^4T_{2g}$ state is around 0.5 eV, the between the two ${}^4T_{1g}$ states, it is 2.1 eV.[42] The splittings are around 0.6 eV and 2.1 eV in the RAS calculations. These three states form two main peaks with separation of ~ 2.0 eV in the RAS calculation, which overlaps very well with the experimental value of ~ 2.1 eV.[42] The separation for $[FeCl_6]^{4-}$ originates from not only ligand field effects, but also electron-electron interactions. The CTM calculation gave a separation energy of ~ 1.9 eV. A DFT calculation with the BP86 functional gave ~ 1.0 eV separation energy.[82]

5.1.2 Hybridization of dipole and quadrupole contributions

Breaking the centrosymmetry will give rise to dipole transitions to the hybridized orbitals, which largely increase the K pre-edge intensity.[42, 43] We

here take $[FeCl_4]^{2-}$ as a typical instance to disentangle the dipole and quadrupole contributions when the symmetry distorts from centrosymmetric O_h to non-centrosymmetric T_d (lack an inversion center). Comparing the experimental K pre-edge spectra, we could see that the total intensity for T_d symmetry $[FeCl_4]^{2-}$ is largely increased. The experimental ratio of total intensity between $[FeCl_4]^{2-}$ and $[FeCl_6]^{4-}$ is $\sim 3.6:1$. The experimental dipole and quadrupole contribution ratio is $\sim 2.3:1$ for $[FeCl_4]^{2-}$, see Table 5.1.

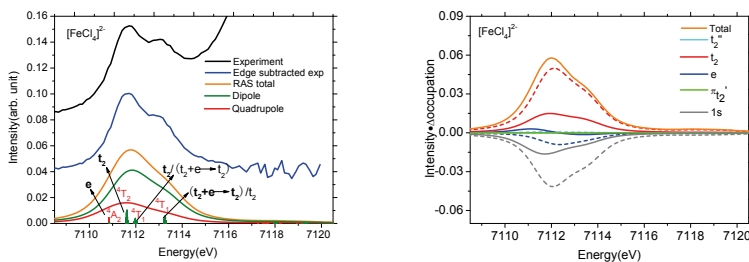


Figure 5.2. Left: Iron K pre-edge XAS of $[FeCl_4]^{2-}$ showing experimental data (black), the edge-subtracted spectra (blue), and RAS results (total: orange, dipole: olive, quadrupole: red). Right: Orbital analyses for the K pre-edge XAS of $[FeCl_4]^{2-}$. Quadrupole contributions are denoted with solid lines while dipole contributions are shown with dashed lines.

The evident features of the K pre-edge for $[FeCl_4]^{2-}$ are two intense peaks and that are split by ~ 1.5 eV.[42] For $[FeCl_4]^{2-}$, the 5E ground state has a $e^3t_2^3$ configuration, electron transition to the e orbital gives the $e^4t_2^3$ excited configuration and produces 4A_2 state. The excited configuration $e^3t_2^4$ gives 4T_1 and 4T_2 states due to the $3d-3d$ electron interactions, see Figure 5.2. Besides, there is a double-excitation state $e^2t_2^4$ that gives another 4T_1 located at higher energy region. The 4T_1 states can mix, and the double excitations can be confirmed from our orbital contribution analysis, see Figure 5.2. These transitions form two pre-edge features split by 1.5 eV in the RAS calculation, which well reproduced the experimental split (1.5 eV), see Table 5.1. The pre-edge energies have information about both ligand-field splitting and orbital covalency, but for a correct interpretation, the effects of configuration interaction with a doubly-excited state needs to be accounted for. DFT gave a splitting energy of ~ 0.7 eV, which was significantly underestimated.

The electric dipole transitions exist in excitations to t_2 orbitals contributing to the total intensity of the K pre-edge, see Figure 5.2. Compared to the total intensity of $[FeCl_6]^{4-}$, the total intensity of $[FeCl_4]^{2-}$ was largely increased. The RAS calculated total intensity ratio between $[FeCl_4]^{2-}$ and $[FeCl_6]^{4-}$ is 3.2:1.0. The calculated intensity ratio between dipole and quadrupole for $[FeCl_4]^{2-}$ is $\sim 2.4:1$. This is difficult to model using the semi-empirical CTM model because adding $4p$ configurations significantly increases the number of fitting parameters, and the intensity is mainly sensitive to the amount of $4p$

mixing. TD-DFT (BP86) includes the effects of orbital hybridization but overestimates the dipole contributions, at least for the current complexes modeled, see Figure 5.3

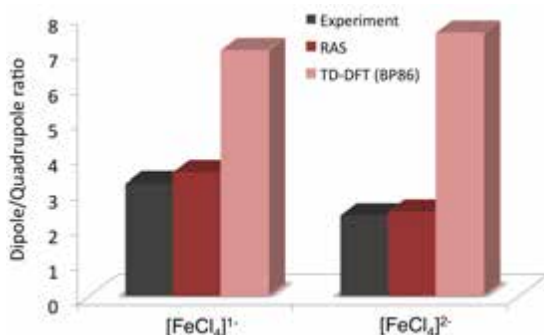


Figure 5.3. The ratio of dipole to quadrupole contributions to the pre-edge area from experiment, RAS and TD-DFT.

5.1.3 Back-donation charge transfer

$[\text{Fe}(\text{CN})_6]^{3-}$ is once again used a σ donation and π back donation model system.[41, 50, 90] There are two peaks in the experimental K pre-edge of $[\text{Fe}(\text{CN})_6]^{3-}$ with intensity ratio of $\sim 1:4.1$,[42] see Figure 5.4. The energy difference between these two peaks is 3.2 eV,[42] which reflects the ligand-field strength, see Table 5.1. In the L-edge XAS,[41, 50] $[\text{Fe}(\text{CN})_6]^{3-}$ has an intense peak that can be assigned to back-donation, see Section 3.2. However, it is not clear whether such features can be detected in K pre-edge spectra, as the back-donation transfer states are usually obscured by the rising edge. The edge-subtracted experimental K pre-edge also predicts another peak ~ 3.9 eV higher than the e_g character peak. This means the charge transfer states still have important contributions to the K pre-edge, and it is necessary to describe the back-donation feature in the K pre-edge calculation.

The ${}^2T_{2g}$ ground state of $[\text{Fe}(\text{CN})_6]^{3-}$ has a $t_{2g}^5 e_g^0$ configuration. A pre-edge peak located at lower energy side is present, which comes from 1s electron excited into the singly occupied t_{2g} orbital, producing a $t_{2g}^6 e_g^0$ configuration and a ${}^1A_{1g}$ state. Another excited configuration is $t_{2g}^5 e_g^1$ after 1s electron excited into e_g orbital. The e_g peak is likely to contain a large contribution from multiplet effects due to the partially filled t_{2g} orbitals, which can complicate multiplet structures of final states through 3d-3d electron interactions. The interactions gave us ${}^3T_{1g}$, ${}^3T_{2g}$, ${}^1T_{1g}$ and ${}^1T_{2g}$ states, as labelled in the Figure 5.4. The difference in energy between the T_{1g} and T_{2g} states probe the difference in attraction between the hole in a d_{xy} orbital and the electron in the d_{z^2} compared to the $d_{x^2-y^2}$.

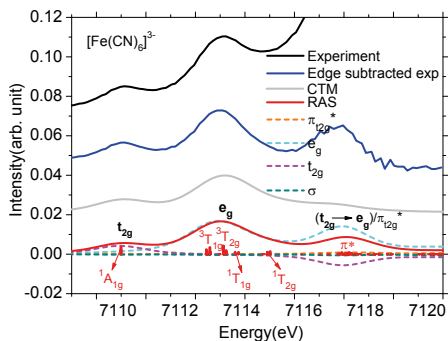


Figure 5.4. Iron K pre-edge XAS $[\text{Fe}(\text{CN})_6]^{3-}$ showing experimental data (black), the edge-subtracted spectra (blue), results from CTM calculations (light gray), and results from RAS calculations (red). Analyses of the valence orbital contributions are shown as dashed lines.

The RAS calculations not only reproduced the 3.2-eV energy difference between the t_{2g} and e_g character peaks but also showed an intensity ratio of 1:4.2 (1:4.1 for experimental result) for these two peaks. The CTM calculation had an energy difference between the t_{2g} and e_g character peaks of about 3.3 eV, and DFT gave a value of 3.5 eV. [82]

In addition to these two peaks, the RAS calculations showed a peak located at 4.0 eV higher compared to the e_g character peak (1.9 eV higher than the ${}^1T_{2g}$ state), which was assigned to a π^* state. The intensity of the π^* state is high, although the contributions of direct excitations to the π^* orbital is very small, as seen from the graphic orbital analysis, see Figure 5.4. The enhanced π^* feature comes from the direct π^* excitation that mixes with a $1s \rightarrow e_g + t_{2g} \rightarrow e_g$ shake-up excitation.[41, 50]. The π^* state was also predicted by the multiplet calculation using an extra electronic configuration $t_{2g}^4 e_g^0$ including π back bonding. For the multiplet calculation, the π^* states are located 3.7 eV higher relative to the e_g character peak with a bit lower intensity compared to the RAS calculation. The DFT gave a separation of $\sim 1.6\text{eV}$ between e_g and MLCT states.[82]

5.1.4 Summary

The RAS calculated K pre-edge intensities have good agreement with the experimental ones, see Figure 5.5. In all three pairs, the pre-edge intensity is higher for the ferric compared to the ferrous complexes. From the linear fit, we could conclude that the RAS method can reproduce intensity differences that come from oxidation state change and coordination number change during a reaction. The RAS calculations reproduced the intensity ratio between dipole and quadrupole contributions, which means the RAS method can prop-

erly model the contributions from electric dipole allowed transitions. It would be important for applications of RAS catalysts with low-symmetry environment.

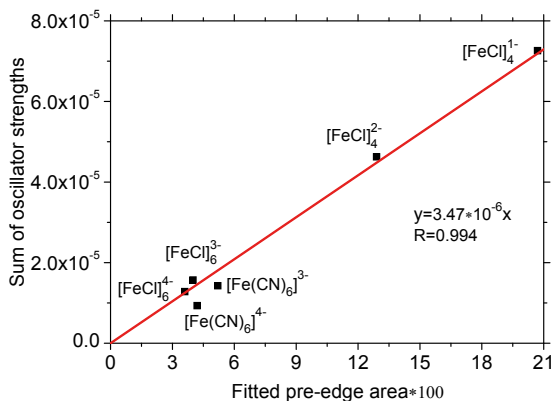


Figure 5.5. Linear fit of the RAS calculated intensities and the experimental K pre-edge intensities obtained from ref.[42].

For the low spin cyanide complexes, experiments predict higher pre-edge intensities than for the six-coordinated chloride complexes, while the calculations predict the opposite relationship. It is surprising if we consider the orbital covalencies, the e_g orbitals are more covalent than weakly bonding t_{2g} orbitals. The low spin complexes have more holes in the e_g orbitals, thus lower intensities are expected. Consequently, both RAS and DFT calculations predict higher intensity for the chloride compared to the cyanide complexes.[82] This means that either the calculations miss an important intensity mechanism, or that the experimental pre-edge areas of the cyanides have been overestimated in reference [42].

5.2 Simulations of the metal 1s2p RIXS of $[Fe(CN)_6]^{n-}$

After successful application of the RAS method on L-edge and K pre-edge XAS simulations, it now is extended to simulate the 1s2p RIXS spectra (Paper VII). As we described in the introduction, the two-photon 1s2p RIXS process can reach the same final-state electron configuration as the L-edge absorption process, see Figure 2.3, and hence can give high-resolution hard X-ray spectra of transition metal complexes. In this chapter, the 1s2p RIXS spectra of back-donation systems $[Fe(CN)_6]^{4-}$ and $[Fe(CN)_6]^{3-}$ are simulated and discussed. The calculated and experimental 1s2p RIXS planes are presented in Figure 5.6,[50] which are plotted in a two-dimensional representation with energy

transfer axis and incident energy axis. The $1s2p$ RIXS spectrum can be further analysed by taking a constant emission energy (CEE) and constant incident energy (CIE) cut, which can be directly compared to metal K pre-edge and the L-edge XAS respectively.

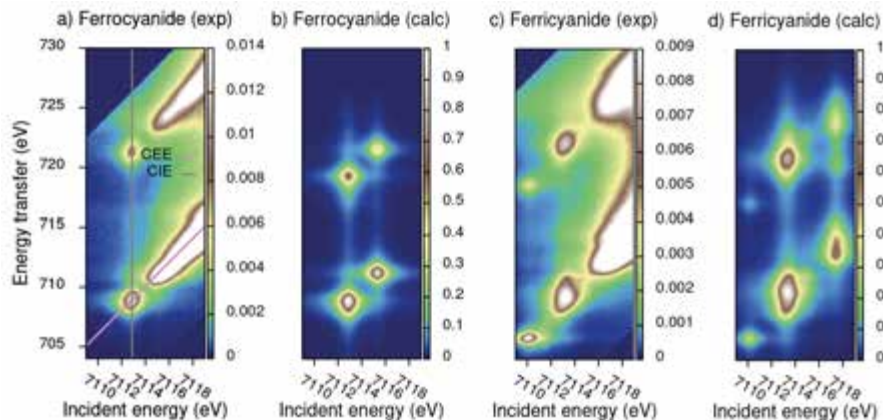


Figure 5.6. The calculated and experimental[50] $1s2p$ RIXS plane of $[Fe(CN)_6]^{4-}$ and $[Fe(CN)_6]^{3-}$.

5.2.1 The $1s2p$ RIXS spectra of $[Fe(CN)_6]^{4-}$

In the experimental RIXS plane of $[Fe(CN)_6]^{4-}$, there is one pre-edge resonance which can be assigned to $1s \rightarrow e_g$ excitation, located at 7112.9 eV in the incident energy direction. The rising edge contributions include a peak at ~ 7115.5 eV and other more intense peaks at higher energy,[50] see Figure 5.6. The calculated $1s2p$ RIXS plane has same general shape as the experimental plane, and exhibits a dominant resonance at 7112.9 eV with a second resonance at 7115.4 eV in the incident energy direction. The second resonance was assigned as a metal-to-ligand back-donation charger transfer transition in the K pre-edge spectrum, which is obscured by the intense rising edge in the experimental plane, see Figure 5.7.

The experiment L_3 edge has two intense peaks at ~ 709.1 eV and ~ 710.7 eV, which can be assigned to e_g and π^* excitation. The L_2 edge also has these two peaks but with smaller intensities, see Figure 5.8.[41] Taking a CIE cut through the dominant resonance at 7112.9 eV can give us an L edge like curve, see gray line in Figure 5.8. Compared to the experiment iron L edge spectrum, the L-edge like spectrum gives a broader e_g character peak and a very weak π^* character peak. The CIE cut from the RAS calculated RIXS spectrum nicely reproduces the spectral difference between RIXS and L-edge XAS, see Figure 5.8. In the CIE cut, the RAS calculation reproduces the change in the width of the e_g resonance with additional intensity at the low-energy side.

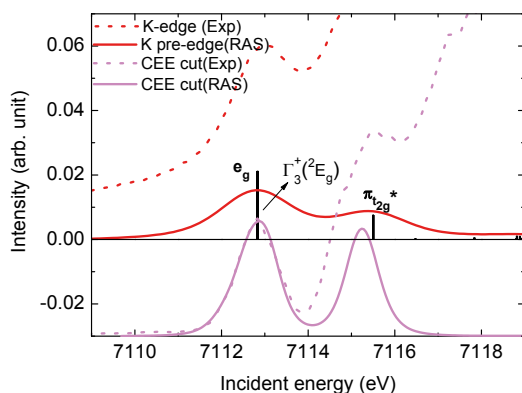


Figure 5.7. Iron K pre-edge XAS spectra with peak assignments and CEE cuts of ferrocyanide $[Fe(CN)_6]^{4-}$ from experiment and RAS calculation.

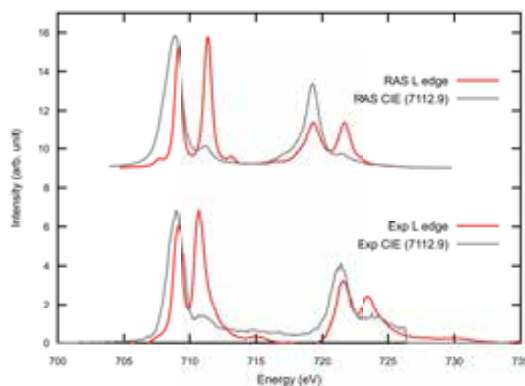


Figure 5.8. The L-edge XAS and CIE cut of $[FeCN_6]^{4-}$.

The broader e_g peak in the L-edge like spectrum can be interpreted by the different transition selection rules for one- and two-photon processes. The $2p^53d^7$ configuration final states have both T_{1u} and T_{2u} symmetry, the one-photon L-edge XAS can only reach the T_{1u} final state while the two-photon RIXS can reach both T_{1u} and T_{2u} states. In the spin-free representation, the simplest linear combination of the T_{1u} and T_{2u} final states can be written $\bar{p}_z d_{z^2}$ and $\bar{p}_z d_{x^2-y^2}$ respectively, where \bar{p}_z represents a hole. For the \bar{p}_z hole the attraction to the d_{z^2} electron is stronger than to a $d_{x^2-y^2}$ electron because of a better overlap if the two orbitals are in the same plane. The T_{2u} states are thus lower in energy because of more favorable 2p-3d electron interaction. It has previously been suggested that the width of the e_g CIE peak is related to the metal-ligand covalency because it measures the relative interaction between a

2p hole localized on the metal and the 3d orbitals involved in bonding. The width of the CIE peak is slightly overestimated in RAS, and the e_g metal-ligand covalency of 65% metal content is also more ionic than reported for the density functional BP86 (57%) or projected from the CTM model (45%).[41]

5.2.2 The 1s2p RIXS spectra of $[Fe(CN)_6]^{3-}$

The experimental 1s2p RIXS spectrum of $[Fe(CN)_6]^{3-}$ gives several pre-edge features. The first sharp t_{2g} character resonance is located at ~ 7110.1 eV. The second resonance is much broader and has a maximum at ~ 7113.3 eV. This resonance is from $1s \rightarrow e_g$ excitations, which are split into many different transitions by exchange, multiplet and spin-orbit interactions, see Figure 5.4. The rising edge with its intense resonances is located at ~ 7117 eV and above, see Figure 5.6. The RAS calculated RIXS plane contains both pre-edge peaks, and also a higher-lying π^* peak that appears as part of the rising edge.[41] The CEE gives significantly sharper spectral features than the K pre edge

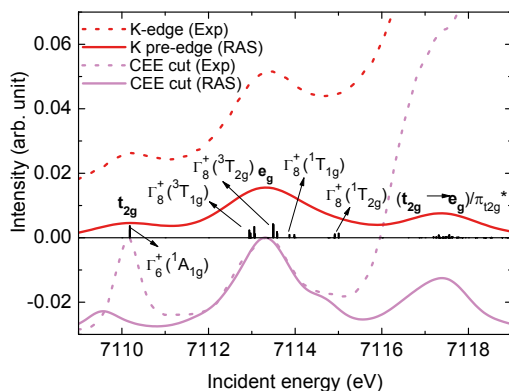


Figure 5.9. Iron K pre-edge XAS spectra with peak assignments and CEE cuts of $[Fe(CN)_6]^{3-}$ from experiment and RAS modeling.

for ferricyanide, especially for the $1s \rightarrow t_{2g}$ resonance, see Figure 5.9. The effect is smaller for the $1s \rightarrow e_g$ peak because it contains a large number of different states, split by exchange, multiplet and spin-orbit interactions in both incident and energy transfer directions. The RAS calculation includes both these features and also a higher-lying π^* peak that appears as part of the rising edge. The description of the e_g peak is good but the intensity of the t_{2g} is underestimated. This is partly due to the underestimation of the intensity of the t_{2g} resonance in the RIXS plane, and partly because the CEE cut goes through a point above the t_{2g} maximum. Shifting the energy of the CEE cut so that it goes through the maximum of the t_{2g} resonance would give a significantly more intense peak.

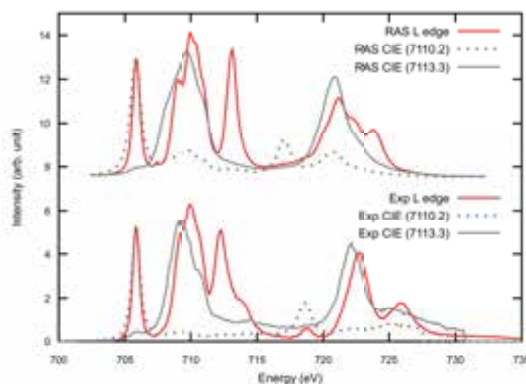


Figure 5.10. The L-edge XAS and CIE cut of $[\text{FeCN}_6]^{3-}$.

The experimental and RAS calculated L-edge XAS are discussed in Section 4.2.1. The CIE cut through the RIXS t_{2g} resonance at 7110.2 eV gives two sharp edges, where the L_2 peak is more intense than in the L-edge XAS. The CIE cut through the e_g resonance at 7113.3 eV shows a broad feature with a width of 2.7 eV in the L_3 edge, see Figure 5.10. Taking the RAS CIE cut through the t_{2g} correctly predicts the increase in intensity of the L_2 edge in the two-photon process. This is due to differences in selection rules in RIXS compared to the L-edge, and this difference cannot be explained without a proper treatment of SOC. This shows that the RAS method correctly takes into account the effects of $3d$, as well as $2p$, SOC in the RAS simulations, see Figure 5.10. The transition from the $J_{3d} = \frac{1}{2}$ ground state to the $J_{2p} = \frac{1}{2}$ final state is allowed in the two-photon RIXS. The CIE cut through the maximum of the e_g resonance is also in agreement with the experimental spectrum. This cut shows intensity at energies below that of the e_g peak in the L-edge, again due to the presence of new final states.[50] As this resonance contains multiple pre-edge resonances, the CIE cuts are sensitive both to the incident and the emission energy, which makes it challenging to assign specific transitions. However, the agreement between RAS and experimental data shows that the RAS method can be used to connect a complicated spectrum to a detailed electronic structure model.

5.2.3 Summary

The RAS simulations have shown that the important spectral effects dominating the spectral shapes are included, e.g., the $2p$ - $3d$ multiplet interaction, the selection rules, both $2p$ and $3d$ SOC. The ferrocyanide results suggest that the $2p$ - $3d$ multiplet interactions are well-reproduced, as seen by the 0.1 eV error in the multiplet broadening of the CIE cut through the main e_g pre-edge

resonance. In ferricyanide, the relative energies of the t_{2g} and e_g pre-edge resonances are reproduced within 0.2 eV. Both examples have centrosymmetry, however, the application of RAS method is not limited to high symmetry. The primary reason for choosing symmetric systems was the possibility to unambiguously identify electronic states and assign transitions. In the previous section, we have already shown that the RAS method can account for 3d-4p orbital hybridization, which makes it possible to apply RAS to model hard X-ray RIXS on low-symmetry (non-centrosymmetry) complexes. The application of RAS method does not have to be restricted to the 1s2p RIXS, it can be applied to other photon processes of interest, e.g., the electron decay to fill 1s hole can be metal 3p orbitals or other ligand character valence orbitals.

6. Conclusion and outlook

In this thesis, the RAS method has been used to simulate and interpret the metal L-edges XAS (Papers I to III), 3d PFY-XAS (Paper IV), K pre-edges (Papers V and VI) and $1s2p$ RIXS (Paper VII) spectroscopies of different manganese and iron complexes. The experimental spectral features are well reproduced in the RAS simulations by including a high-level description of 2p and 3d SOC, ligand field, multiplet effects, $3d - 4p$ orbital hybridization, selection rules, as well as charge transfer between metal and ligands. These results make RAS an attractive method to model different X-ray spectroscopies of metal catalysts, particularly for the catalysts in solution environment.

More specifically, the splitting between the L_3 and L_2 edge is underestimated by ~ 1.0 eV ($\sim 10\%$ of the 2p SOC magnitude), it might be related to the orbital optimization scheme in the RAS calculation. To avoid the 2p core orbital rotation with high-lying 3p orbitals, the 2p core orbitals have been frozen in the RAS calculation. The deviation constantly exists in all the RAS calculation of metal L edge spectra, and the relative energies of different peaks can deliver more useful information. Apart from 2p SOC, an accurate description of 3d SOC is also essential for the modeling of metal L-edge XAS spectra. In the low spin Fe^{3+} case, accounting for 3d SOC leads to visible changes, which are connected to differences in selection rules for the different SOC states. In the $Fe^{II}(P)$, the 3d SOC is also required to describe the potential mixing among low-lying states of different multiplicity.

The RAS method can provide an accurate way to describe multiplet structures, which are important to shape the metal L-edge spectra. Through comparison of the metal L-edge XAS of $[Fe(CN)_6]^n$ and $[Fe(P)(ImH)_2]^n$ complexes, the spectral fingerprints in oxidation state and ligand environment are observed and discussed. The RAS calculations and similarity analyses of the metal L-edge XAS with different low-lying spin states are performed on $Fe(P)$, the accuracy gives us confidence to use RAS simulations to fingerprint the different spin states based on their spectral features. The combination of experimental measurements of beam damage free 3d PFY-XAS and RAS spectra simulations on $Mn^{II}(acac)_2$ and $Mn^{III}(acac)_3$ paves a route to understand the electronic structure of Mn_4CaO_5 cluster in photosystem II. This is done by connecting to spin and charge density differences between ground state and excited state to spectral shape and incident energy shift.

In the K pre-edge XAS, the multiplet structures might be obscured by the large natural bandwidth, but with RIXS experiment can reach high resolution in the energy transfer direction. Therefore, it becomes necessary to describe

the multiplet structures in the hard X-ray region. In the example of $[FeCl_6]^{4-}$, the K pre-edge XAS gives a two-peak feature, which is separated by not only ligand field effects, but also electron-electron interactions, which is confirmed by the RAS calculation and orbital contribution analysis. An important intensity mechanism for K pre-edge XAS is $3d-4p$ orbital hybridization, the distortion from centrosymmetry can give rise to electric dipole transitions in the K pre-edge region due to metal $4p$ orbital component delocalization into the valence $3d$ orbital. It is essential to be able to estimate the dipole contributions to correctly predict spectral effects when a catalyst site changes during a reaction. The RAS method enables calculations of the metal K pre-edge XAS intensities in the length representation and makes it adequate for systems containing more than one transition metal element.

The charge transfer between metal and ligands can be described by including important ligand character orbitals in the active space. For example, with back-donation orbitals in the active space, the MLCT features are observed in metal L-edge, K pre-edge and $1s2p$ RIXS of the ferrous- and ferricyanide complexes. With π donation orbitals in the active space for $Fe^{II}(P)(ImH)_2$, the LMCT features at low energy side of L_3 edge can be well described. For the $3d$ PFY-XAS spectra calculations of Mn complexes in this thesis, the charge transfer contributions are small, and the RAS calculations can reproduce the major experimental spectra features without including the ligand character orbitals in the active space.

The applications in this thesis show that RAS can be extended from small to medium size of systems by proper selections of active space, basis set and computational algorithms. For the metal L-edge and K pre-edge spectra, the core orbitals use one of three RAS sub-spaces, which leaves flexibility in the design of the valence orbitals in another two RAS sub-space for lowering the computational cost. In the $1s2p$ RIXS calculation, two different types of core orbitals are included in two RAS sub-spaces, which leaves no room to design the valence active space. In this case, the limitation can potentially be addressed by using a generalized active space approach, which can include more sub-spaces.[111–113] However, it remains challenging to apply RAS method on multi-metal complexes, which require a large number of active orbitals to deal with electron correlations. The density matrix renormalization group technique can largely decrease the cost for large active space (up to 40 active orbitals),[114–116] which make it a promising method to deal with complicated systems, such as multi-metal Mn_4CaO_5 cluster in photosystem II.[117] The developments of these techniques allow us to use them in the future X-ray spectroscopy calculation and interpretation.

7. Sammanfattning på svenska

Många kemiska reaktioner är beroende av effektiva katalysatorer gjorda av övergångsmetaller. En viktig utmaning för ett framtida hållbart energisystem är att kunna omvandla solenergin till kemisk energi i bränslen, t ex vätgas eller metanol. Ett exempel på en välfungerande katalysator är växternas fotosyntes som effektivt katalyserar uppdelningen av vatten till syre med hjälp av mangan. Molekylära katalysatorer baserade på järn, koppar och mangan är ideala kandidater för att ersätta de ämnen som idag används så som iridium och platinium, vilka inte är hållbara tillgångsmässigt. De syntetiska katalysatorer som finns idag är dock inte tillräckligt effektiva och bryts ned alldeles för lätt. För att framställa bättre katalysatorer är det viktigt att på detaljerad nivå kunna studera deras struktur och egenskaper.

En vanlig metod för att undersöka en katalysators egenskaper är att se vilken typ av synligt ljus den absorberar. Den metoden är dock svår att använda för många system eftersom det synliga ljuset kan absorberas i andra delar systemet än just den katalytiska metallen. För att komma runt det problemet används röntgenstrålning. Varje grundämne absorberar strålning som har tillräckligt med energi för att excitera en elektron från ett av de inre elektronskalerna. Genom att anpassa strålningens energi kan man fokusera på den övergångsmetall som utgör den aktiva delen av katalysatorn. Med röntgenspektroskopi kan man till exempel undersöka strukturen av olika katalytiska centra, oxidationstillstånd, och metall-ligand bindningen. Olika typer av spektroskopi får fram olika information om systemet och det är i stort systemets omgivning som avgör vilken spektroskopi som kan användas.

Metallprotein och metallkomplex i lösning har traditionellt studerats med hårdröntgen eftersom den inte absorberas så starkt av omgivningen. Utvecklingen av intensiva röntgenkällor som frielektronlasrar samt nya effektiva detektorer gör det nu möjligt att studera sådana system med högupplöst mjukröntgenstrålning. Framstegen för de experimentella metoderna leder till behov av teoretiska modeller som kan tolka den nya informationen. Avhandlingen presenterar framsteg i modellering av röntgenspektra med Restricted Active Space (RAS), som är baserad på en korrekt beskrivning av den kvantmekaniska vågfunktionen. Metoden har använts för att analysera mjukröntgenspektra och på vilket sätt de kan användas för att studera metallers elektronstruktur. Dessutom beskrivs en utvidgning av metoden för att beskriva även hårdröntgenspektra. Det gör att samma metod nu kan användas för att beskriva samtliga röntgenabsorptionsprocesser som används för katalysatorer i lösning.

RAS-metoden kan, med god precision, ta hänsyn till alla viktiga faktorer som beskriver röntgenspektra för bundna tillstånd: multiplettstruktur, spinnban-koppling samt metall-ligand interaktioner. Flera modellmolekyler, prototyper för de större katalytiska systemen, har använts för att testa RAS-metodens överensstämmelse med experiment och dess förmåga att särskilja komplex utifrån dess elektronstruktur. Generellt är RAS-metoden väldigt flexibel i vilka system den kan hantera. Det baseras på iden av att det går att få ut god precisionen jämfört med tyngre elektronkonfigurationsinteraktionsberäkningar, genom att välja ut de orbitaler som är viktiga för röntgenprocessen, och låta alla elektronkonfigurationer interagera inom det rummet. Olika typer av röntgenspektroskopiska processer kan beskrivas, om rätt orbitaler väljs och fördelas på rätt sätt i det aktiva rummet.

Med hjälp RAS-metoden har röntgenspektret från L-absorptionskanten, som beskriver excitation från 2p till 3d orbitalerna, undersökts för $[Fe^{II/III}(CN)_6]^{4-/3-}$ i två olika oxidationstillstånd, tvåvärt och trevärt. De två systemen fungerar som modell för σ -donation och π -bakdonation. Effekterna av multiplettstrukturen, π bakåtdonerings-effekten, samt spinnban-koppling kan beskrivas med hög noggrannhet. Flera tester har gjorts för att undersöka hur känsliga resultaten är för detaljer i RAS beräkningarna. Simuleringar har också gjorts för L-absorptionskanten på hemjärn som är en viktig komponent i flera viktiga enzymer, t ex hemoglobin som transporterar syre. Hemjärn har samma typ av metall-ligand bindning som $[Fe(CN)_6]^{n-}$ och skillnaderna i röntgenspektra kan användas för att närmare studera hur liganderna påverkar elektronstrukturen hos järn. RAS-beräkningar har dessutom utförts för att visa hur metallers L-absorptionskant kan vara kraftfulla prober för att identifiera en elektronkonfigurationen från dessa spektroskopiska "fingeravtryck". Ett första steg har också tagits för att kvantitativt jämföra likheten mellan experimentella och teoretiskt beräknade röntgenspektra.

För att bidra till förståelsen kring hur manganklustret som oxiderar vatten till syrgas i växternas fotosyntes kan studeras har två mangansystem med olika oxidationstillstånd, $Mn^{II}(acac)_2$ och $Mn^{III}(acac)_3$, studerats med L-kantsabsorptionsspektra som detekteras med partiell fluorescens. Genom RAS-beräkningar diskuteras hur skillnaderna i experimentella resultat mellan komplex med olika formella oxidationstal kan relateras till förändringarna i spin- och laddningstäthet.

Utvecklingen av RAS-metoden har möjliggjort de första RAS beräkningarna av hårdröntgenexcitation från 1s till 3d orbitaler, just före K-absorptionskanten. Det har skett bortom dipolapproximationen genom att implementera en approximativt ursprungsberoende beräkning av övergångarnas intensitet som inkluderar bland annat elektrisk kvadrupol och magnetisk dipol. Återigen diskuteras spektret för de centrosymmetriska komplexen $[Fe(CN)_6]^{n-}$ som modellsystem för σ -donation och π -bakdonation. Intensiteten för övergångarna ökar signifikant om centrosymmetrin bryts, till exempel när systemet är tetraedriskt koordinerat som i $[FeCl_4]^-$. Detta möjliggör för hybridisering mellan 3d och

4p orbitaler, vilket i sin tur leder till att urvalsregler som tidigare förbjöd dipolövergångar nu hävs och dessa övergångar kan observeras även före den verkliga K-absorptionskanten. Att kunna beskriva effekten av symmetriändringar är avgörande för att studera en katalysprocess där geometrin ändras under reaktionen.

Ett problem med övergångarna i K-kanten är att de högenergitalstånd som skapas efter röntgenabsorption är väldigt kortlivade. Enligt kvantmekanikens osäkerhetsprincip blir då övergångarnas energi svårbestämda och detaljer går förlorade. För att ge högupplösta detaljer om elektronstrukturen i energiområdet för hård röntgenstrålning används tvåfotonprocessen resonant inelastisk röntgenspridning. Den specifika process som studerats har samma sluttillstånd som L-absorptionskanten men med olika urvalsregler. Båda experimenten beskrivs väl av RAS och användandet av molekylorbitalteori visar hur skillnaderna mellan experimenten kan användas för att få en detaljerad bild av orbitalerna.

Sammantaget beskriver avhandlingen framsteg i hur den multikonfigurationella vågfunktionsmetoden RAS kan användas för att simulera, tolka och även förutsäga experimentella resultat, oavsett vilken typ av röntgenspektroskopi som är av intresse. Genom detaljerad information om vilka elektronkonfigurationer som ingår i en specifik vågfunktion kan röntgenspektra förklaras utifrån ett och samma teoretiska ramverk. I framtida studier är målet att använda dessa metoder för att med god säkerhet identifiera reaktiva tillstånd samt analysera vilka faktorer som är viktiga för att uppnå effektiv katalys.

Acknowledgements

I never realized four-years PhD life goes so fast until I come to this section, scenes of the first days still clearly rose before my eyes. I feel so lucky to have the opportunity to study in Sweden, and meet so many great people, and experience different culture during this journey. I would sincerely thank all people come to my life, there is no chance to arrive the destination of my PhD journal without your support, encouragement and care.

First and foremost I would like to express warmest gratitude to my supervisor, the best of the best, **Marcus Lundberg**, for bringing me to Sweden, guiding me to the field of X-ray spectroscopy, and encouraging me to build internal and external collaborations with different groups. It is luxury to have so many meetings and discussions with you, I really enjoyed every discussion and learned a lot from you, thanks very much for your remarkable patience. The course of 'Theory of transition metal' lectured by you is the best course I have attended, I benefit really a lot from this course, you should make it public for more students.

I would like to thank my co-supervisor and the group leader **Roland Lindh**, for your dedication to building positive, creative and loving working environment, make us work as a team, even family. I keep in mind the words 'We do serious science' you said at the first day we met.

I would like to thank **Rongxing He**, who introduced me to theoretical chemistry as first initiation teacher, thanks for your continuous encouragement throughout my years of PhD study, and thanks for your advice in my study and life.

I would like to appreciate the help from colleagues **Erik Källman** and **Lasse Kragh Sørensen**, who shared me the invaluable ideas on the projects we have done, and comments on my thesis.

I am also grateful to all the former and present member in the theoretical chemistry group, **Ignacio Fernández Galván**, **Morgane Vacher**, **Hans Karlsson**, **Nessima Salhi**, **Rahul V. Pinjari**, **Esko Makkonen**, **Liqin Xue**, **Michael Stenrup**, **Pooria Farahani**, **Charlotta Bengtson**, **Dennis Caldwell**, **Orlando Tapia**, **Mickaël G Delcey**, **Martin Agback**, **Piotr Froelich**, and many others, who shared many happiness in the FIKA and lunch time.

The collaboration between **Philippe Wernet**, **Markus Kubin** from Helmholtz Zentrum Berlin triggered my interest in the the X-ray experiment, and I really learned a lot from our hundreds of email conversion and discussions, and also thanks very much for your host when I was at BESSYII. Thank **Junko Yano**, **Uwe Bergmann** for your support in the position application process,

thank you and **Thomas Kroll** for the invaluable instructions in the beamtime at LCLS, which are helpful for me to understand more about the X-ray experiments, especially thank **Thomas Fransson** for the discussions and help during the beamtime. Thank **Leif Hammarström, Tianfei Liu** for involving me in your interesting project, I have enjoyed working with you.

I would never survive the PhD life without fresh air outside lab. A warm thank you to **Chengyu Wang, Jing Chen, Ylva Gardenia Wang** and cute **Bao sisters** for your hospitality and delicious foods in the weekends, your meticulous care make me feel being at home here, I will definitely miss the desserts made by **Bao**. Thank **Shixiong Xu, Cici, Yohan, Patrick, Brigitte, Laura, and Jian Ren** for the good time we had during my traveling and visiting.

To my Chinese friends who are and were in Sweden, **Fengzhen Sun, Wenxing Yang, Feiyan Liang, Shunguo Wang, Lichuan Wu, Yi Ren, Weijia Yang, Song Chen, Dou Du, Ligu Wang, Jieying Cui, Shihuai Wang, Jiefang Zhu, Shuainan Zhao, Zhaohui Wang, Hailiang Fang, Chengyu Wen, Shuangshuang Zeng, Mingzhi Jiao, Chengjun Wu, Liyang Shi, Jiaojiao Yang, Changqing Ruan, Jiajie Yan, Gang Duan, Lin Li, Lei Zhang, Jinwen Song, Jun Luo, Chenjuan Liu, Teng Zhang, Yongmei Gong, Shu Li, Xiaowen Li**, it is so nice to meet all you here, thanks for all the happiness and delicious foods we shared together.

At the final stage, I would like to express my profound gratitude to my parents and sisters, you are always there for me, thanks for the infinite understanding and support. I would like to say a heartfelt 'thank you' to the most special person, my beloved girlfriend, **Yuhan Ma**, thank you for being here for the last year of my PhD study, it is the biggest support to me. I love you!

References

- [1] Nicola Armaroli and Vincenzo Balzani. The future of energy supply: challenges and opportunities. *Angewandte Chemie International Edition*, 46(1-2):52–66, 2007.
- [2] Harun Tüysüz and Candace K Chan. *Solar energy for fuels*. Springer, 2016.
- [3] John Whitmarsh et al. The photosynthetic process. In *Concepts in Photobiology*, pages 11–51. Springer, 1999.
- [4] Nathan Nelson and Charles F Yocum. Structure and function of photosystems i and ii. *Annu. Rev. Plant Biol.*, 57:521–565, 2006.
- [5] James Barber. Photosynthetic energy conversion: natural and artificial. *Chemical Society Reviews*, 38(1):185–196, 2009.
- [6] Devens Gust, Thomas A Moore, and Ana L Moore. Solar fuels via artificial photosynthesis. *Accounts of Chemical Research*, 42(12):1890–1898, 2009.
- [7] Tomoji Kawai and Tadayoshi Sakata. Conversion of carbohydrate into hydrogen fuel by a photocatalytic process. *Nature*, 286(5772):474–476, 1980.
- [8] Nathan S Lewis and Daniel G Nocera. Powering the planet: Chemical challenges in solar energy utilization. *Proceedings of the National Academy of Sciences*, 103(43):15729–15735, 2006.
- [9] Akihiko Kudo and Yugo Miseki. Heterogeneous photocatalyst materials for water splitting. *Chemical Society Reviews*, 38(1):253–278, 2009.
- [10] Kazuhiko Maeda and Kazunari Domen. Photocatalytic water splitting: recent progress and future challenges. *The Journal of Physical Chemistry Letters*, 1(18):2655–2661, 2010.
- [11] Eugen S Andreiadis, Murielle Chavarot-Kerlidou, Marc Fontecave, and Vincent Artero. Artificial photosynthesis: From molecular catalysts for light-driven water splitting to photoelectrochemical cells. *Photochemistry and Photobiology*, 87(5):946–964, 2011.
- [12] Savio JA Moniz, Stephen A Shevlin, David James Martin, Zheng-Xiao Guo, and Junwang Tang. Visible-light driven heterojunction photocatalysts for water splitting—a critical review. *Energy & Environmental Science*, 8(3):731–759, 2015.
- [13] Pingwu Du and Richard Eisenberg. Catalysts made of earth-abundant elements (co, ni, fe) for water splitting: recent progress and future challenges. *Energy & Environmental Science*, 5(3):6012–6021, 2012.
- [14] Vincent Artero, Murielle Chavarot-Kerlidou, and Marc Fontecave. Splitting water with cobalt. *Angewandte Chemie International Edition*, 50(32):7238–7266, 2011.
- [15] Isolda Roger and Mark D Sypes. First row transition metal catalysts for solar-driven water oxidation produced by electrodeposition. *Journal of Materials Chemistry A*, 4(18):6724–6741, 2016.
- [16] Junko Yano and Vittal K Yachandra. X-ray absorption spectroscopy. *Photosynthesis Research*, 102(2-3):241, 2009.

- [17] Wolfgang Gudat and Christof Kunz. Close similarity between photoelectric yield and photoabsorption spectra in the soft-x-ray range. *Physical Review Letters*, 29(3):169, 1972.
- [18] Simon Schreck, Gianina Gavrilă, Christian Weniger, and Philippe Wernet. A sample holder for soft x-ray absorption spectroscopy of liquids in transmission mode. *Review of Scientific Instruments*, 82(10):103101, 2011.
- [19] Maria Ekimova, Wilson Quevedo, Manfred Faubel, Philippe Wernet, and Erik T.J. Nibbering. A liquid flatjet system for solution phase soft-x-ray spectroscopy. *Structural Dynamics*, 2(5):054301, 2015.
- [20] Rolf Mitzner, Jens Rehanek, Jan Kern, Sheraz Gul, Johan Hattne, Taketo Taguchi, Roberto Alonso-Mori, Rosalie Tran, Christian Weniger, Henning Schröder, et al. L-edge x-ray absorption spectroscopy of dilute systems relevant to metalloproteins using an x-ray free-electron laser. *The Journal of Physical Chemistry Letters*, 4(21):3641–3647, 2013.
- [21] David Attwood. Soft x-rays and extreme ultraviolet radiation. *Soft X-Rays and Extreme Ultraviolet Radiation*, by David Attwood, pp. 486. ISBN 0521652146. Cambridge, UK: Cambridge University Press, August 1999., page 486, 1999.
- [22] Kathrin M Lange and Emad F Aziz. Electronic structure of ions and molecules in solution: a view from modern soft x-ray spectroscopies. *Chemical Society Reviews*, 42(16):6840–6859, 2013.
- [23] Pieter Glatzel and Uwe Bergmann. High resolution 1s core hole x-ray spectroscopy in 3d transition metal complexes-electronic and structural information. *Coordination Chemistry Reviews*, 249(1):65–95, 2005.
- [24] Ida Josefsson, Kristjan Kunnus, Simon Schreck, Alexander Föhlisch, Frank de Groot, Philippe Wernet, and Michael Odellius. Ab initio calculations of x-ray spectra: Atomic multiplet and molecular orbital effects in a multiconfigurational scf approach to the l-edge spectra of transition metal complexes. *The Journal of Physical Chemistry Letters*, 3(23):3565–3570, 2012.
- [25] Nicholas Engel, Sergey I Bokarev, Edlira Suljoti, Raul Garcia-Diez, Kathrin M Lange, Kaan Atak, Ronny Golnak, Alexander Kothe, Marcus Dantz, Oliver Kühn, et al. Chemical bonding in aqueous ferrocyanide: experimental and theoretical x-ray spectroscopic study. *The Journal of Physical Chemistry B*, 118(6):1555–1563, 2014.
- [26] Sergey I Bokarev, Munirah Khan, Mahmoud K Abdel-Latif, Jie Xiao, Rifaat Hilal, Saadullah G Aziz, Emad F Aziz, and Oliver Kühn. Unraveling the electronic structure of photocatalytic manganese complexes by l-edge x-ray spectroscopy. *The Journal of Physical Chemistry C*, 119(33):19192–19200, 2015.
- [27] Philippe Wernet, Kristjan Kunnus, Ida Josefsson, Ivan Rajkovic, Wilson Quevedo, Martin Beye, Simon Schreck, Sebastian Grübel, Mirko Scholz, Dennis Nordlund, et al. Orbital-specific mapping of the ligand exchange dynamics of $\text{Fe}(\text{CO})_5$ in solution. *Nature*, 520(7545):78, 2015.
- [28] Friedrich Hund et al. Linienspektren und periodisches system der elemente. 1927.
- [29] Tanabe Yukito Sugano Satoru and Kamimura Hiroshi. *Multiplets of transition-metal ions in crystals*. Academic Press inc. New York, 1970.

- [30] Hermann Arthur Jahn and Edward Teller. Stability of polyatomic molecules in degenerate electronic states. i. orbital degeneracy. In *Proceedings of the Royal Society of London A: Mathematical, Physical and Engineering Sciences*, volume 161, pages 220–235. The Royal Society, 1937.
- [31] Malcolm Gerloch and Edwin C Constable. *Transition metal chemistry: the valence shell in d-block chemistry*. Wiley Online Library, 1994.
- [32] Ryutaro Tsuchida. Absorption spectra of co-ordination compounds. i. *Bulletin of the Chemical Society of Japan*, 13(5):388–400, 1938.
- [33] Ryutaro Tsuchida. Absorption spectra of co-ordination compounds. ii. *Bulletin of the Chemical Society of Japan*, 13(6):436–450, 1938.
- [34] Ryutaro Tsuchida and Masahisa Kobayashi. Absorption spectra of co-ordination compounds. iii. special bands of chromium complexes. *Bulletin of the Chemical Society of Japan*, 13(7):471–480, 1938.
- [35] Hisao Kuroya and Ryutaro Tsuchida. Absorption spectra of co-ordination compounds. iv. ethylenediamine cobaltic complexes. *Bulletin of the Chemical Society of Japan*, 15(10):427–439, 1940.
- [36] Ward Jesse, Ollmann Emily, Maxey Evan, and A. Finney. Lydia. *X-Ray Absorption Spectroscopy of Metalloproteins*, pages 171–187. Humana Press:Springer, New York, NY(USA), 2014. ISBN 978-1-62703-794-5.
- [37] Pieter Glatzel, Uwe Bergmann, Junko Yano, Hendrik Visser, John H Robblee, Weiwei Gu, Frank MF de Groot, George Christou, Vincent L Pecoraro, Stephen P Cramer, et al. The electronic structure of mn in oxides, coordination complexes, and the oxygen-evolving complex of photosystem ii studied by resonant inelastic x-ray scattering. *Journal of the American Chemical Society*, 126(32):9946–9959, 2004.
- [38] Kari L Stone, Rachel K Behan, and Michael T Green. X-ray absorption spectroscopy of chloroperoxidase compound i: insight into the reactive intermediate of p450 chemistry. *Proceedings of the National Academy of Sciences of the United States of America*, 102(46):16563–16565, 2005.
- [39] Junko Yano, Jan Kern, Kenneth Sauer, Matthew J Latimer, Yulia Pushkar, Jacek Biesiadka, Bernhard Loll, Wolfram Saenger, Johannes Messinger, Athina Zouni, et al. Where water is oxidized to dioxygen: structure of the photosynthetic mn₄ca cluster. *Science*, 314(5800):821–825, 2006.
- [40] Junko Yano and Vittal Yachandra. Mn₄ca cluster in photosynthesis: where and how water is oxidized to dioxygen. *Chemical Reviews*, 114(8):4175–4205, 2014.
- [41] Rosalie K Hocking, Erik C Wasinger, Frank MF de Groot, Keith O Hodgson, Britt Hedman, and Edward I Solomon. Fe l-edge xas studies of k₄ [fe (cn) 6] and k₃ [fe (cn) 6]: a direct probe of back-bonding. *Journal of the American Chemical Society*, 128(32):10442–10451, 2006.
- [42] Tami E Westre, Pierre Kennepohl, Jane G DeWitt, Britt Hedman, Keith O Hodgson, and Edward I Solomon. A multiplet analysis of fe k-edge 1s→3d pre-edge features of iron complexes. *Journal of the American Chemical Society*, 119(27):6297–6314, 1997.
- [43] Serena DeBeer George, Patrick Brant, and Edward I Solomon. Metal and ligand k-edge xas of organotitanium complexes: Metal 4p and 3d contributions to pre-edge intensity and their contributions to bonding. *Journal of the*

- American Chemical Society*, 127(2):667–674, 2005.
- [44] Takashi Yamamoto. Assignment of pre-edge peaks in k-edge x-ray absorption spectra of 3d transition metal compounds: electric dipole or quadrupole? *X-Ray Spectrometry*, 37(6):572–584, 2008.
- [45] AL Roe, DJ Schneider, RJ Mayer, JW Pyrz, J Widom, and L Que Jr. X-ray absorption spectroscopy of iron-tyrosinate proteins. *Journal of the American Chemical Society*, 106(6):1676–1681, 1984.
- [46] Jan-Uwe Rohde, Theodore A Betley, Timothy A Jackson, Caroline T Saouma, Jonas C Peters, and Lawrence Que. Xas characterization of a nitridoiron (iv) complex with a very short fe- n bond. *Inorganic chemistry*, 46(14):5720–5726, 2007.
- [47] Manfred Otto Krause and JH Oliver. Natural widths of atomic k and l levels, k α x-ray lines and several kll auger lines. *Journal of Physical and Chemical Reference Data*, 8(2):329–338, 1979.
- [48] Frank De Groot. High-resolution x-ray emission and x-ray absorption spectroscopy. *Chemical Reviews*, 101(6):1779–1808, 2001.
- [49] P Glatzel, M Sikora, and M Fernandez-Garcia. Resonant x-ray spectroscopy to study k absorption pre-edges in 3d transition metal compounds. *The European Physical Journal-Special Topics*, 169(1):207–214, 2009.
- [50] Marcus Lundberg, Thomas Kroll, Serena DeBeer, Uwe Bergmann, Samuel A Wilson, Pieter Glatzel, Dennis Nordlund, Britt Hedman, Keith O Hodgson, and Edward I Solomon. Metal–ligand covalency of iron complexes from high-resolution resonant inelastic x-ray scattering. *Journal of the American Chemical Society*, 135(45):17121–17134, 2013.
- [51] Thomas Kroll, Ryan G Hadt, Samuel A Wilson, Marcus Lundberg, James J Yan, Tsu-Chien Weng, Dimosthenis Sokaras, Roberto Alonso-Mori, Diego Casa, Mary H Upton, et al. Resonant inelastic x-ray scattering on ferrous and ferric bis-imidazole porphyrin and cytochrome c: Nature and role of the axial methionine–fe bond. *Journal of the American Chemical Society*, 136(52):18087–18099, 2014.
- [52] Luuk JP Ament, Michel Van Veenendaal, Thomas P Devereaux, John P Hill, and Jeroen Van Den Brink. Resonant inelastic x-ray scattering studies of elementary excitations. *Reviews of Modern Physics*, 83(2):705, 2011.
- [53] Björn O Roos, Peter R Taylor, Per EM Siegbahn, et al. A complete active space scf method (casscf) using a density matrix formulated super-ci approach. *Chemical Physics*, 48(2):157–173, 1980.
- [54] Björn O Roos and KP Lawley. Ab initio methods in quantum chemistry ii. *Advances in Chemical Physics*, 69:399–446, 1987.
- [55] Jeppe Olsen, Björn O Roos, Poul Jørgensen, and Hans Jørgen Aa Jensen. Determinant based configuration interaction algorithms for complete and restricted configuration interaction spaces. *The Journal of Chemical Physics*, 89(4):2185–2192, 1988.
- [56] Michael W Schmidt and Mark S Gordon. The construction and interpretation of mscf wavefunctions. *Annual Review of Physical Chemistry*, 49(1):233–266, 1998.
- [57] Björn O Roos, Kerstin Andersson, Markus P Fülcher, Per Åke Malmqvist, Luis Serrano-Andrés, Kristin Pierloot, and Manuela Merchán.

- Multiconfigurational perturbation theory: Applications in electronic spectroscopy. *Advances in Chemical Physics: New Methods in Computational Quantum Mechanics, Volume 93*, pages 219–331, 2007.
- [58] Per Åke Malmqvist, Alistair Rendell, and Björn O Roos. The restricted active space self-consistent-field method, implemented with a split graph unitary group approach. *Journal of Physical Chemistry*, 94(14):5477–5482, 1990.
- [59] Max Born and Robert Oppenheimer. Zur quantentheorie der molekeln. *Annalen der Physik*, 389(20):457–484, 1927.
- [60] Charlotte Froese Fischer. General hartree-fock program. *Computer Physics Communications*, 43(3):355–365, 1987.
- [61] Per-Olov Löwdin. Quantum theory of many-particle systems. iii. extension of the hartree-fock scheme to include degenerate systems and correlation effects. *Physical review*, 97(6):1509, 1955.
- [62] Kerstin Andersson, Per Åke Malmqvist, Björn O Roos, Andrzej J Sadlej, and Krzysztof Wolinski. Second-order perturbation theory with a casscf reference function. *Journal of Physical Chemistry*, 94(14):5483–5488, 1990.
- [63] Kerstin Andersson, Per-Åke Malmqvist, and Björn O Roos. Second-order perturbation theory with a complete active space self-consistent field reference function. *The Journal of Chemical Physics*, 96(2):1218–1226, 1992.
- [64] Per Åke Malmqvist, Kristine Pierloot, Abdul Rehaman Moughal Shahi, Christopher J Cramer, and Laura Gagliardi. The restricted active space followed by second-order perturbation theory method: Theory and application to the study of cuo2 and cu2o2 systems. *The Journal of Chemical Physics*, 128(20):204109, 2008.
- [65] James Finley, Per-Åke Malmqvist, Björn O Roos, and Luis Serrano-Andrés. The multi-state caspt2 method. *Chemical Physics Letters*, 288(2):299–306, 1998.
- [66] Per Åke Malmqvist, Björn O Roos, and Bernd Schimmelpfennig. The restricted active space (ras) state interaction approach with spin-orbit coupling. *Chemical Physics Letters*, 357(3):230–240, 2002.
- [67] Marvin Douglas and Norman M Kroll. Quantum electrodynamical corrections to the fine structure of helium. *Annals of Physics*, 82(1):89–155, 1974.
- [68] Björn O Roos, Roland Lindh, Per Åke Malmqvist, Valera Veryazov, and Per-Olof Widmark. Main group atoms and dimers studied with a new relativistic ano basis set. *The Journal of Physical Chemistry A*, 108(15):2851–2858, 2004.
- [69] Björn O Roos, Roland Lindh, Per-Åke Malmqvist, Valera Veryazov, and Per-Olof Widmark. New relativistic ano basis sets for transition metal atoms. *The Journal of Physical Chemistry A*, 109(29):6575–6579, 2005.
- [70] Per Åke Malmqvist and Björn O Roos. The casscf state interaction method. *Chemical Physics Letters*, 155(2):189–194, 1989.
- [71] Stephan Bernadotte, Andrew J Atkins, and Christoph R Jacob. Origin-independent calculation of quadrupole intensities in x-ray spectroscopy. *The Journal of Chemical Physics*, 137(20):204106, 2012.
- [72] Hendrik A Kramers and Werner Heisenberg. Über die streuung von strahlung durch atome. *Zeitschrift für Physik A Hadrons and Nuclei*, 31(1):681–708, 1925.

- [73] M-A Arrio, Stéphanie Rossano, Ch Brouder, L Galois, and G Calas. Calculation of multipole transitions at the Fe K pre-edge through pd hybridization in the ligand field multiplet model. *EPL (Europhysics Letters)*, 51(4):454, 2000.
- [74] Frank De Groot. Multiplet effects in x-ray spectroscopy. *Coordination Chemistry Reviews*, 249(1):31–63, 2005.
- [75] Y Joly. X-ray absorption near-edge structure calculations beyond the muffin-tin approximation. *Physical Review B*, 63(12):125120, 2001.
- [76] John J Rehr, Joshua J Kas, Fernando D Vila, Micah P Prange, and Kevin Jorissen. Parameter-free calculations of x-ray spectra with feff9. *Physical Chemistry Chemical Physics*, 12(21):5503–5513, 2010.
- [77] Hans Ågren, Vincenzo Carravetta, Olav Vahtras, and Lars GM Pettersson. Direct, atomic orbital, static exchange calculations of photoabsorption spectra of large molecules and clusters. *Chemical Physics Letters*, 222(1-2):75–81, 1994.
- [78] L Triguero, LGM Pettersson, and H Ågren. Calculations of near-edge x-ray-absorption spectra of gas-phase and chemisorbed molecules by means of density-functional and transition-potential theory. *Physical Review B*, 58(12):8097, 1998.
- [79] J Vinson, JJ Rehr, JJ Kas, and EL Shirley. Bethe-salpeter equation calculations of core excitation spectra. *Physical Review B*, 83(11):115106, 2011.
- [80] Andris Gulans, Stefan Kontur, Christian Meisenbichler, Dmitrii Nabok, Pasquale Pavone, Santiago Rigamonti, Stephan Sagmeister, Ute Werner, and Claudia Draxl. Exciting: a full-potential all-electron package implementing density-functional theory and many-body perturbation theory. *Journal of Physics: Condensed Matter*, 26(36):363202, 2014.
- [81] Ulf Ekström, Patrick Norman, Vincenzo Carravetta, and Hans Ågren. Polarization propagator for x-ray spectra. *Physical Review Letters*, 97(14):143001, 2006.
- [82] Serena DeBeer George, Taras Petrenko, and Frank Neese. Prediction of iron k-edge absorption spectra using time-dependent density functional theory. *The Journal of Physical Chemistry A*, 112(50):12936–12943, 2008.
- [83] Arto Sakko, Angel Rubio, Mikko Hakala, and Keijo Hämäläinen. Time-dependent density functional approach for the calculation of inelastic x-ray scattering spectra of molecules. *The Journal of Chemical Physics*, 133(17):174111, 2010.
- [84] P Chandrasekaran, S Chantal E Stieber, Terrence J Collins, Lawrence Que Jr, Frank Neese, and Serena DeBeer. Prediction of high-valent iron k-edge absorption spectra by time-dependent density functional theory. *Dalton Transactions*, 40(42):11070–11079, 2011.
- [85] Frederico A Lima, Ragnar Bjornsson, Thomas Weyhermüller, Perumalreddy Chandrasekaran, Pieter Glatzel, Frank Neese, and Serena DeBeer. High-resolution molybdenum k-edge x-ray absorption spectroscopy analyzed with time-dependent density functional theory. *Physical Chemistry Chemical Physics*, 15(48):20911–20920, 2013.
- [86] G Capano, TJ Penfold, NA Besley, CJ Milne, M Reinhard, H Rittmann-Frank, P Glatzel, R Abela, U Rothlisberger, M Chergui, et al. The role of

- hartree–fock exchange in the simulation of x-ray absorption spectra: a study of photoexcited [Fe(bpy)₃]²⁺. *Chemical Physics Letters*, 580:179–184, 2013.
- [87] Michael Roemelt, Dimitrios Maganas, Serena DeBeer, and Frank Neese. A combined dft and restricted open-shell configuration interaction method including spin-orbit coupling: Application to transition metal l-edge x-ray absorption spectroscopy. *The Journal of Chemical Physics*, 138(20):204101, 2013.
- [88] Michael Roemelt and Frank Neese. Excited states of large open-shell molecules: an efficient, general, and spin-adapted approach based on a restricted open-shell ground state wave function. *The Journal of Physical Chemistry A*, 117(14):3069–3083, 2013.
- [89] Dimitrios Maganas, Michael Roemelt, Thomas Weyhermüller, Raoul Blume, Michael Hävecker, Axel Knop-Gericke, Serena DeBeer, Robert Schlögl, and Frank Neese. L-edge x-ray absorption study of mononuclear vanadium complexes and spectral predictions using a restricted open shell configuration interaction ansatz. *Physical Chemistry Chemical Physics*, 16(1):264–276, 2014.
- [90] Rosalie K Hocking, Erik C Wasinger, Yi-Long Yan, Frank MF deGroot, F Ann Walker, Keith O Hodgson, Britt Hedman, and Edward I Solomon. Fe l-edge x-ray absorption spectroscopy of low-spin heme relative to non-heme Fe complexes: Delocalization of Fe d-electrons into the porphyrin ligand. *Journal of the American Chemical Society*, 129(1):113–125, 2007.
- [91] Karl M Kadish, Kevin M Smith, and Roger Guilard. *The Porphyrin Handbook: Inorganic, organometallic and coordination chemistry*, volume 3. Elsevier, 2000.
- [92] Shigeru Obara and Hiroshi Kashiwagi. A binitio mo studies of electronic states and mössbauer spectra of high-, intermediate-, and low-spin Fe(II)-porphyrin complexes. *The Journal of Chemical Physics*, 77(6):3155–3165, 1982.
- [93] Yoong-Kee Choe, Takahito Nakajima, Kimihiko Hirao, Roland Lindh, et al. Theoretical study of the electronic ground state of iron(II) porphine. ii. *Journal of Chemical Physics*, 111(9):3837–3845, 1999.
- [94] Kristine Pierloot, Quan Manh Phung, and Alex Domingo. Spin state energetics in first-row transition metal complexes: Contribution of (3s3p) correlation and its description by second-order perturbation theory. *Journal of Chemical Theory and Computation*, 13(2):537–553, 2017.
- [95] André R Groenhof, Marcel Swart, Andreas W Ehlers, and Koop Lammertsma. Electronic ground states of iron porphyrin and of the first species in the catalytic reaction cycle of cytochrome p450s. *The Journal of Physical Chemistry A*, 109(15):3411–3417, 2005.
- [96] Meng-Sheng Liao, John D Watts, and Ming-Ju Huang. Assessment of the performance of density-functional methods for calculations on iron porphyrins and related compounds. *Journal of computational chemistry*, 27(13):1577–1592, 2006.
- [97] Samuel A Wilson, Thomas Kroll, Richard A Decreau, Rosalie K Hocking, Marcus Lundberg, Britt Hedman, Keith O Hodgson, and Edward I Solomon. Iron l-edge x-ray absorption spectroscopy of oxy-picket fence porphyrin: experimental insight into Fe–O₂ bonding. *Journal of the American Chemical*

- Society*, 135(3):1124–1136, 2013.
- [98] Sergey I Bokarev, Marcus Dantz, Edlira Suljoti, Oliver Kühn, and Emad F Aziz. State-dependent electron delocalization dynamics at the solute-solvent interface: soft-x-ray absorption spectroscopy and ab initio calculations. *Physical Review Letters*, 111(8):083002, 2013.
- [99] Kaan Atak, Sergey I Bokarev, Malte Gotz, Ronny Golnak, Kathrin M Lange, Nicholas Engel, Marcus Dantz, Edlira Suljoti, Oliver Kühn, and Emad F Aziz. Nature of the chemical bond of aqueous Fe^{2+} probed by soft x-ray spectroscopies and ab initio calculations. *The Journal of Physical Chemistry B*, 117(41):12613–12618, 2013.
- [100] Margareta RA Blomberg and Per EM Siegbahn. A comparative study of high-spin manganese and iron complexes. *Theoretical Chemistry Accounts*, 97(1-4):72–80, 1997.
- [101] Melissa M Grush, Yasuji Muramatsu, JH Underwood, Eric M Gullikson, David L Ederer, Rupert CC Perera, and Thomas A Callcott. Soft x-ray emission and absorption a comparative study on the sensitivity to oxidation state and ligand environment of transition metal complexes. *Journal of electron spectroscopy and related phenomena*, 92(1):225–229, 1998.
- [102] Laura Gagliardi, Roland Lindh, and Gunnar Karlström. Local properties of quantum chemical systems: The lprop approach. *The Journal of Chemical Physics*, 121(10):4494–4500, 2004.
- [103] Robert S Mulliken. Electronic population analysis on lcao–mo molecular wave functions. i. *The Journal of Chemical Physics*, 23(10):1833–1840, 1955.
- [104] Axel D Becke. Becke’s three parameter hybrid method using the lyp correlation functional. *The Journal of Chemical Physics*, 98:5648–5652, 1993.
- [105] Chengteh Lee, Weitao Yang, and Robert G Parr. Development of the colle-salvetti correlation-energy formula into a functional of the electron density. *Physical Review B*, 37(2):785, 1988.
- [106] Seymour H Vosko, Leslie Wilk, and Marwan Nusair. Accurate spin-dependent electron liquid correlation energies for local spin density calculations: a critical analysis. *Canadian Journal of Physics*, 58(8):1200–1211, 1980.
- [107] PJ Stephens, FJ Devlin, CFn Chabalowski, and Michael J Frisch. Ab initio calculation of vibrational absorption and circular dichroism spectra using density functional force fields. *The Journal of Physical Chemistry*, 98(45):11623–11627, 1994.
- [108] Mikael P Johansson, Margareta RA Blomberg, Dage Sundholm, and Mårten Wikström. Change in electron and spin density upon electron transfer to haem. *Biochimica et Biophysica Acta (BBA)-Bioenergetics*, 1553(3):183–187, 2002.
- [109] D Van der Marel, GA Sawatzky, and FU Hillebrecht. Direct observation of the exchange-split virtual bound state in dilute mn alloys. *Physical review letters*, 53(2):206, 1984.
- [110] Loig Vaugier, Hong Jiang, and Silke Biermann. Hubbard u and hund exchange j in transition metal oxides: Screening versus localization trends from constrained random phase approximation. *Physical Review B*, 86(16):165105, 2012.
- [111] Dongxia Ma, Giovanni Li Manni, and Laura Gagliardi. The generalized active space concept in multiconfigurational self-consistent field methods. *The*

- Journal of Chemical Physics*, 135(4):044128, 2011.
- [112] Konstantinos D Vogiatzis, Giovanni Li Manni, Samuel J Stoneburner, Dongxia Ma, and Laura Gagliardi. Systematic expansion of active spaces beyond the casscf limit: a gasscf/splitgas benchmark study. *Journal of Chemical Theory and Computation*, 11(7):3010–3021, 2015.
- [113] Dongxia Ma, Giovanni Li Manni, Jeppe Olsen, and Laura Gagliardi. Second-order perturbation theory for generalized active space self-consistent-field wave functions. *Journal of Chemical Theory and Computation*, 12(7):3208–3213, 2016.
- [114] Garnet Kin-Lic Chan and Sandeep Sharma. The density matrix renormalization group in quantum chemistry. *Annual review of physical chemistry*, 62:465–481, 2011.
- [115] Dominika Zgid and Marcel Nooijen. The density matrix renormalization group self-consistent field method: Orbital optimization with the density matrix renormalization group method in the active space. *The Journal of chemical physics*, 128(14):144116, 2008.
- [116] Yuki Kurashige and Takeshi Yanai. Second-order perturbation theory with a density matrix renormalization group self-consistent field reference function: Theory and application to the study of chromium dimer. *The Journal of chemical physics*, 135(9):094104, 2011.
- [117] Yuki Kurashige, Garnet Kin-Lic Chan, and Takeshi Yanai. Entangled quantum electronic wavefunctions of the mn4cao5 cluster in photosystem ii. *Nature chemistry*, 5(8):660–666, 2013.

Acta Universitatis Upsaliensis

*Digital Comprehensive Summaries of Uppsala Dissertations
from the Faculty of Science and Technology 1541*

Editor: The Dean of the Faculty of Science and Technology

A doctoral dissertation from the Faculty of Science and Technology, Uppsala University, is usually a summary of a number of papers. A few copies of the complete dissertation are kept at major Swedish research libraries, while the summary alone is distributed internationally through the series Digital Comprehensive Summaries of Uppsala Dissertations from the Faculty of Science and Technology. (Prior to January, 2005, the series was published under the title “Comprehensive Summaries of Uppsala Dissertations from the Faculty of Science and Technology”.)



ACTA
UNIVERSITATIS
UPSALIENSIS
UPPSALA
2017

Distribution: publications.uu.se
urn:nbn:se:uu:diva-328072